Estimation of Global Scale Carbon Fluxes Using Maximum Likelihood Ensemble Filter

K. M. P. Perera[1*], R. S. Lokupitiya[1], A. S. Denning[2], P. K. Patra[3], D. Zupanski[4], M. Zupanski[5], R. G. N. Meegama[6], E. Y. K. Lokupitiya[7], I. Baker[2], D. Baker[5], T. Machida[8], H. Matsueda[9], Y. Sawa[9,10], Y. Niwa[8]

[1]Department of Statistics, University of Sri Jayewardenepura, Sri Lanka. [2]Department of Atmospheric Science, Colorado State University, Fort Collins, Colorado, USA. [3]Research Institute for Global Change, JAMSTEC, Yokohama, 236-0001, Japan. [4]Zupanski Consulting, LLC, Fort Collins, CO, USA. [5]Cooperative Institute for Research in the Atmosphere, Colorado State University, Fort Collins, CO, USA. [6]Department of Computer Science, University of Sri Jayewardenepura, Sri Lanka. [7]Department of Zoology and Environment Sciences, University of Colombo, Sri Lanka. [8]Center for Global Environmental Research (CGER), National Institute for Environmental Studies (NIES), Japan. [9]Oceanography and Geochemistry Research Department, Meteorological Research Institute, Tsukuba, Japan. [10]Global Environment and Marine Department, Japan Meteorological Agency

Manjula Perera (manjula@sjp.ac.lk)

Key Points:

- Densely observed regions showed comparable results with CarbonTracker (CT2017) and other similar studies.
- MLEF seems to perform well with high dimensional CO_2 observation vectors such as satellite and aircraft measurements.
- CO_2 fluxes were poorly recovered in the regions having few measurement sites.

Abstract

Inverse modelling method named Maximum likelihood Ensemble Filter (MLEF) was used to estimate gridded surface CO_2 fluxes using continuous, flask and Comprehensive Observation Network for TRace gases by AIrLiner (CONTRAIL) data for the years 2009-2011. Here, MLEF coupled with Parametric Chemistry Transport Model (PCTM) driven by Modern-Era Retrospective analysis for Research and Applications, Version 2 (MERRA2) weather data has been used. Flux estimation was done by solving separate multiplicative biases for photosynthesis, respiration, and air-sea gas exchange fluxes. Hourly land fluxes derived from Simple Biosphere-version 3 (SiB3) model, Takahashi ocean fluxes and Brenkert fossil fuel emissions were used as the prior fluxes. The inversion was carried out by assimilating hourly CO_2 observations, According to this study, North America showed about 60-80% uncertainty reduction while the Asian and European regions showed moderate results with 50-60% uncertainty reduction. Most other land and oceanic regions showed less than 30% uncertainty reduction. The results were mainly compared with well-known CarbonTracker and some parallel inversion studies by considering long-term averages of the estimated fluxes for the TransCom regions. Boreal North America, Temperate North America and Australia showed similar annual averages in each case. Tropical Asia and Europe showed comparable results with all other studies except for the CarbonTracker. The biases were poorly constrained in the regions having few measurement sites like South America, Africa and Eurasian Temperate which showed completely different result with other studies.

1 Introduction

Carbon is an essential component for all life on earth and atmospheric carbon exists mainly as the carbon dioxide (CO_2) gas. It is the single largest contributor to the global warming among well-mixed greenhouse gases. The rapid increasing patterns in atmospheric CO_2 concentration may lead to significant global climatic changes in the coming years. CO_2 concentration in the atmosphere has shown a significant increase by 30% since 1950 (Al-Ghussain, 2018) which is mainly due to the increasing human activities after industrial revolution. According to Le Quere et al. (2018), fossil fuel combustion, cement production and gas flaring are the main sources of CO_2. In order to make policy decisions on CO_2 emissions, there are several gatherings and agreements among different countries and they need the knowledge of regional and country level carbon fluxes to make policies on carbon emission. As a result, research on global carbon cycle using different approaches to identify the spatiotemporal distribution of carbon sources and sinks has become popular topic among researchers in the field.

Top-down atmospheric inversions and bottom-up biosphere models are the two main fundamentally different approaches used in estimating carbon fluxes. Bottom-up biosphere models typically simulate the atmosphere-terrestrial biosphere exchange based on the understanding of complex exchange processes such as photosynthesis, respiration, decomposition, land-use change emissions, fire emissions, etc. Another approach to estimate biospheric CO_2 fluxes is the "top-down" estimation technique which uses the inverse modelling method. This method estimate net CO_2 flux by the assimilating atmospheric CO_2 measurements from global network using a transport model, with the prior information such as net land flux, net ocean flux, fire emissions, and fossil fuel emissions. In literature, many studies were carried out to infer regional sources and sinks by using inverse methods (Baker et al., 2006; Basu et al., 2014; Bruhwiler et al., 2005; Gurney et al., 2002; Jiang et al., 2013; Kim et al., 2014; Kim et al., 2017; Lokupitiya et al., 2008; Michalak et al., 2004; Patra et al., 2012; Peters et al., 2005; Peylin et al., 2013; Piao, et al., 2009, 2013; Rödenbeck et al., 2003; Saeki et al., 2013; Tans et

al., 1990). But still they need more advanced knowledge on statistics and mathematics while obtaining the accurate estimates.

Many researchers have discussed the advantages and disadvantages in both methods. According to Chatterjee et al. (2012), in top-down approach the estimated fluxes are mainly based on atmospheric CO_2 concentrations and it does not get the knowledge on biogeochemical processes associated with the carbon cycle as it is possible by the bottom-up approaches. And this may be a disadvantage of the method. Kondo et al. (2019) has highlighted potential difficulties faced by CO_2 budget assessment methods based on above two approaches and suggested several ways to obtain more robust estimates. According to the used top-down atmospheric inverse models and biosphere models in their study, it was found that there were no optimal combination of models of atmospheric inversions and biosphere models that are capable of producing consistent budget estimates for all global regions. They have identified that one reason for this variability is as the possibility of some modelling issues such as differences in prior fluxes, model resolution, size of the control vector, data assimilation window length, the rate of transporting CO_2 concentrations from a source region to neighbouring regions through atmospheric transport model and the transport model errors. Other than above reasons, variations in the measurement error covariance matrix and the prior flux and its error covariance matrix also affect considerable differences in CO_2 flux measurements (Sajeev et al., 2019). According to Kondo et al. (2019), the next main reason is the dipole effect in the design of inversion systems. It was also mentioned in their study that the poor representation of some processes such as forest regrowth, crop land harvesting and management, wood harvesting and degradation in the biosphere models may greatly affect the regional budget estimates while using the bottom-up approach.

Earlier, atmospheric CO_2 measurements are mainly collected by in-situ measurement sites, ships and aircrafts. Top-down inverse modelling based on Bayesian synthesis or batch mode inversion is the most commonly used approach to estimate CO_2 sources and sinks. However, limited number of CO_2 measurements makes the inverse problem both under-determined and ill-posed (Chatterjee, 2012). Although, the large region inversions were developed (Gurney et al., 2002) to over-come this problem, it may lead to aggregation errors (Kaminski et al., 2001). The surface sites measurements have high precision and they are mostly located in remote areas with limited spatial coverage. In order to get accurate estimates in inverse modelling, the spatial and temporal characteristics provided by the observed CO_2 measurements are highly important while running the transport model. The densely observed CO_2 observation network is more important in accurately estimating the surface carbon sources and sinks at finer grid scale in atmospheric inversions. The existing observation network is partially compensated by newly available satellite observations and increasingly by aircraft measurements (Niwa et al., 2012). Compared to research aircrafts, passenger aircraft CO_2 measurements can be done at a much lower cost and could cover large areas (Jiang et al., 2014) and those are collected under two projects namely, the Civil Aircraft for the Regular Investigation of the atmosphere Based on an Instrument Container (CARIBIC) and Comprehensive Observation Network for Trace gases by Airliner (CONTRAIL) since 2005 (Machida et al., 2008; Matsueda et al., 2008) which provide a large coverage of in situ CO_2 data ranging over various latitudes, longitudes, and altitudes. According to Niwa et al. (2011) vertical CO_2 profiles measured by aircrafts provide new constraints on surface flux estimation. The Greenhouse Gases Observing Satellite (GOSAT) in January 2009 and the Orbiting Carbon Observatory-2 (OCO-2) satellite in 2014 was launched by National Aeronautics and Space Administration (NASA), Atmospheric CO_2 observations from space (ACOS) project to capture the CO_2 global distribution at a finer spatial and temporal resolution. The CO_2 measurements collected under various platforms (eg. surface

measurements, CONTRAIL and satellites CO_2 measurements) need the help of statistical analysis to accurately estimate the global carbon fluxes in more finer spatial-temporal resolution in inverse modelling. This large amount of atmospheric CO_2 measurements require advanced data assimilation methods to obtain improved estimates at finer scales in inverse modelling (Chatterjee, 2012). In order to address the increasing computational challenges in atmospheric inverse modelling an alternative assimilation techniques for the batch inversions such as Ensemble Kalman Filter (EnKF) (Chatterjee et al., 2012; Feng et al., 2009; Kang et al., 2011; Kim et al., 2014; Miyazaki et al., 2011; Peters et al., 2005, 2007), variational methods (Baker et al., 2006; Basu et al., 2013) and hybrid approaches such as Maximum Likelihood Ensemble Filter (MLEF; Lokupitiya et al., 2008; Zupanski et al., 2007) have been used by the carbon research community to estimate carbon fluxes.

Although the literature is rich on inverse modelling studies using flask and continuous measurements, only few studies have focused on CO_2 flux estimation using CONTRAIL CO_2 measurements with advanced data assimilation methods. Bayesian synthesis inversion has been applied in carbon flux estimation with newly available CONTRAIL CO_2 data in many studies (Jiang et al., 2014; Niwa et al., 2012). Niwa et al. (2012) has performed an inversion study using CONTRAIL measurements in addition to the surface measurement data set (GLOBALEVIEW-CO2). They have estimated regional monthly surface fluxes using the Bayesian synthesis approach for the period 2006-2008 using the Nonhydrostatic Icosahedral Atmosphere Model-based Transport Model and 64% of error reduction were obtained for tropical Asia regions. Jiang et al. (2014) also used Bayesian synthesis approach with TM5 transport model to obtain flux estimates for China using CONTRAIL observations during 2002-2008. The results of the study showed that carbon sink in China has increased due to the effect of adding new CONTRAIL CO_2 data and it has decreased the carbon sink in South and Southeast Asia. There are few number of studies used ensemble data assimilation method and obtained satisfactory results (Miyasaki et al., 2011, Zhang et al., 2014) with CONTRAIL CO_2 measurements in carbon flux estimation. An inverse modelling system based on CarbonTracker frame work was used by Zhang et al. (2014) to estimate the carbon flux for Asia by introducing CONTRAIL CO_2 measurements and shown that adding CONTRAIL CO_2 can reduce the uncertainty by 11% over the Asian region. Patra et al. (2011) conducted an inversion using CARIBIC data with GLOBALVIEW-CO_2 for year 2008 and simulated CO_2 were evaluated with CONTRAIL CO_2 measurements. In this study, TDI64 time-dependent inverse model and ACTM forward transport simulations were used for the flux estimation. During 2008, it was identified that the net CO_2 uptake of 0.37 ± 0.20 Pg C yr^{-1} by the South Asian region. Miyazaki et al. (2011) has developed an advanced 4-D data assimilation system based on (Ensemble Kalman Filter) EnKF with a 3 day assimilation window to estimate surface CO_2 fluxes at model grid point using three types of atmospheric measurements such as GOSAT, CONTRAIL and ground surface. According to the results of this study, a large flux error reductions in the continental areas of the northern extra tropics were occurred due to surface network data and GOSAT contributed to a large error reduction over North and South America, South Africa, and Temperate and Boreal Asia. And the large error reduction over Europe and Tropical and Temperate Asia were due to CONTRAIL data.

As described above, only a handful of studies have been done in the past on global scale CO_2 fluxes. In the current study, we estimate the global scale carbon fluxes for years 2009-2011 by using an ensemble-based data assimilation system known as MLEF (Lokupitiya et al., 2008; Zupanski, 2005; Zupanski et al., 2007). The method have been tested for existing flask and in-situ CO_2 observations using a pseudodata experiment by Lokupitiya et al. (2008). MLEF is an ensemble based data assimilation method based on maximum likelihood and Ensemble data

assimilation and it has the capability of handling large observational vectors. Not like in variational data assimilation method (Baker et al., 2006, Chevallier et al., 2005) it can be used with non-linear observation operators and no need to calculate model adjoints (i.e. calculation of backward-in-time transport). Fixed-lag Kalman smoother introduced by Bruhwiler et al. (2005), steps through the observations sequentially, avoids the difficulties of using large observation vectors in batch mode method. But pre-calculation of observation operators is much expensive when assimilating hourly large observation vectors (Lokupitiya et al., 2008). The optimal solution obtained using other ensemble data assimilation methods is a minimum variance solution but MLEF gives an optimal solution based on maximum likelihood solution. Since, MLEF algorithm is based on maximum likelihood estimation the additional calculation required for the iterative minimization can be negligible, compared to the cost of ensemble forecast and Hessian preconditioning calculations (Zupanski, 2005). This property provides a grate advantage for data assimilation problems with large observation vectors like CONTRAIL CO_2 data. Serial processing of observations is not used in covariance localization under MLEF method. Like other ensemble data assimilation methods, MLEF uses ensembles in calculating error covariance matrix and these ensembles efficiently calculate Hessian preconditioning and the gradient of the cost function. Multiple process capability of parallel computing is used in order to optimize the MLEF performance in realistic applications and this significantly reduced the computational cost (Zupanski, 2005). When comparing with computational cost, both variational and ensemble methods are similar. But the great advantage of the ensemble method is that it is more efficient in parallel computing environment (Lokupitiya et al., 2008). This study is the first time, the MLEF algorithm is used in the inverse modelling approach with CONTRAIL CO_2 measurements.

In this study, MLEF algorithm was developed to assimilate CONTRAIL measurements. We have previously tested this assimilation system in a pseudodata experiment by considering the in-situ CO_2 measurement network and CONTRAIL observations (Perera et al., 2017). We obtained satisfactory results for the densely observed regions such as North America, Europe and Asia. This paper presents the first application of the MLEF method to recover fluxes by using the actual CO_2 measurements from flasks, continuous sites and CONTRAIL. The optimized CO_2 fluxes by assimilating the actual flask, continuous and CONTRAIL CO_2 measurements were obtained for the years from 2009 to 2011. We compared our results with those of CarbonTracker (Peters et al., 2005, 2007, CT2017 release at https://www.esrl.noaa.gov/gmd/ccgg/carbontracker/CT2017/).

The paper is organized as follows. Method is described in Section 2. MLEF data assimilation method and observation vector used for the data assimilation are discussed here. In section 3, we present and compare our results with pervious findings. Finally, section 4 provides the concluding remarks and future directions.

2 Materials and Methods

2.1 MLEF

The MLEF has been developed by combining ideas from variational methods, iterated Kalman filters, and the ensemble transform Kalman filter (Lokupitiya et al., 2008; Zupanski, 2005). Unlike other ensemble-based methods, the MLEF incorporates iterative minimization of a non-linear cost function with advanced Hessian preconditioning, which makes it more robust for non-linear processes. The method is based on maximum likelihood (rather than minimum

variance) estimation and thus the optimal solution is given by the mode (rather than the mean) of the posterior distribution. Hence the MLEF can produce robust estimates even when the flux distribution deviates from the Gaussian assumption, as shown in Zupanski et al. (2007).

2.2 Atmospheric Transport Model

Inverse modeling for carbon fluxes requires a transport model to simulate 3-D CO_2 concentrations, from which we sample the CO_2 at the locations (i.e. for a specific latitude, longitude and elevation) and times of the observations. This serves as the observation operator in the data assimilation scheme. The observation operator performs the necessary interpolations and transformations from the state variable to the observation space.

In this study, we used the Parameterized Chemistry Transport Model (PCTM) (Kawa et al., 2004) driven by weather data from the MERRA2 meteorological fields based on the Goddard Earth Observation System Model, version 2, by the NASA Global Modeling and Assimilation Office (GAMO). The PCTM model has been used in CO_2 assimilation studies as an observation operator by Lokupitiya et al. (2008) and Zupanski (2005) and showed reasonable results with continuous and flask CO_2 measurements. Perera et al. (2017) compared the model results with CONTRAIL measurements in addition to the existing flask and continuous measurements and showed similar results for the carbon flux estimation in densely observed areas.

All the data collections from MERRA2 are provided on the same horizontal grid which has 576 points in the longitudinal direction and 361 points in the latitudinal direction, corresponding to a resolution of 0.625°×0.5°. In MERRA2 the variables are provided on vertical grid with 72 model layers or the 73 edges, in the altitude range of 0-50 km. The weather data files (three-hourly time-averaged files) contain averages over time intervals centered and time stamped at 01:30 GMT, 04:30 GMT, and 07:30 GMT (Bosilovich et al., 2016).

In this study, the PCTM was run at 2.5° longitude by 2.0° latitude horizontal resolution with 25 vertical levels, in the altitude range of 0-22 km. The model integration time step was chosen as 15 minutes. The resolution of the wind and diagonals, which are derived from MERRA2 weather product, have been regridded to coarser 2.5°×2.0° resolution.

2.3 Data Assimilation scheme

2.3.1 Mathematical formulation of the carbon flux

We estimated multiplicative biases in photosynthesis, respiration, and air-sea gas exchange using our data assimilation system. Variations of the surface flux of CO_2 can be mathematically represented across each of our assimilation windows as follows:

$$F(x,y,t) = [1+\beta_{RESP}(x,y)]RESP(x,y,t) - [1+\beta_{GPP}(x,y)]GPP(x,y,t) + [1+\beta_{Ocean}(x,y)]Ocean(x,y,t) + FF(x,y,t), \quad (1)$$

where, *F*- carbon flux, *RESP* is the ecosystem respiration, *GPP* is the gross primary productivity, *Ocean* represents air-sea gas exchange of CO_2, and FF represents emissions due to fossil fuel combustion; *x* and *y* denote the spatial coordinates and *t* represents the time. The **β**'s represent multiplicative biases of the grid-scale component fluxes which are assumed to persist for longer periods of time than the fluxes themselves (Lokupitiya et al., 2008; Schuh et al., 2010; Zupanski et al., 2007). Equation (1) represents the optimization for a given data

assimilation cycle. Here we do not include the time (*t*) variable for **β**'s because they are assumed to be constant within the data assimilation cycle. Hourly land fluxes (*RESP* and *GPP*) are derived at each grid cell from the Simple Biosphere-version 3 (SiB3) model (Baker et al., 2003). Ocean fluxes are from Takahashi et al. (2002) and fossil fuel (*FF*) emissions from Brenkert (1998). Mean annual *FF* emissions of 1998 were linearly scaled for the years 2009, 2010 and 2011 to produce the *FF* maps. We did not include biomass burning in our priors; hence the impact from biomass burning is embedded in the other flux estimates. Biases are solved for at a coarser 2.5° longitude by 2° latitude spatial resolution, whereas fluxes and transport are gridded at 2.5° longitude by 2° latitude spatial resolution. At the coastlines, grid boxes are assigned to either land or ocean based on the percentage of coverage. The coarser grid for biases is chosen to reduce the number of unknowns in the problem.

Here we solve for monthly variations of biases in *GPP*, *RESP*, and *Ocean* fluxes ($\boldsymbol{\beta}_{GPP}$, $\boldsymbol{\beta}_{RESP}$, $\boldsymbol{\beta}_{Ocean}$) and for the purpose of this paper, we assume that $\boldsymbol{\beta}_{FF} = 0$. Trial values for the different ensemble runs at every model grid cell in each of these three flux components are selected from a distribution to construct a global map of the **β**'s for each ensemble member. These maps of **β's** are then multiplied by the flux computed from the forward model at each model time step that the transport operator (PCTM) is applied and then sampled to yield an ensemble of CO_2 mixing ratio time series at each observation station associated with each candidate map. An eight-week time series of hourly observations is thereby constructed for each ensemble member, after which time optimal values of the biases are estimated for each grid cell by comparison to the real observations.

Simulated variations of *GPP(x,y,t)* and *RESP(x,y,t)* due to diurnal, synoptic, and seasonal variations are explicitly represented using mechanistic models, and spatially resolved multiplicative biases are separately estimated for each component flux. Sub-daily variations in the simulated component fluxes *RESP* and *GPP* are primarily controlled by the weather (especially changes in radiation due to clouds and the diurnal cycle of solar forcing), whereas seasonal changes are derived from phenological calculations parameterized from satellite imagery. Fine scale spatial variations are driven by changes in vegetation cover, soil texture, and soil moisture. A persistent bias in photosynthesis might result (for example) from underestimation of available nitrogen, forest management, or agricultural land-use, whereas a persistent bias in respiration might result from overestimation of soil carbon or coarse woody debris. In any case, it is reasonable to assume that the biases $\boldsymbol{\beta}_{RESP}$ and $\boldsymbol{\beta}_{GPP}$ vary more slowly than the fluxes themselves.

2.3.2 Data assimilation window

Size of the data assimilation window represents how far back in time we expect to be able to locate a given flux signal from available measurements (CT2017 release at https://www.esrl.noaa.gov/gmd/ccgg/carbontracker/CT2017/). In this study, an 8-week data assimilation window is used for the estimation of the **β**'s, and each 8-week window overlaps the previous window by 4 weeks.

2.3.3 Initial guess of the biases and propagation of the error covariance matrix

The data assimilation process has been started from the unbiased case (i.e. $\boldsymbol{\beta}s = \mathbf{0}$). Prior uncertainty for land components (*GPP/RESP*) and ocean are prescribed as 20% and 10%, respectively, at the first data assimilation cycle at the starting time. Here, these are applied

separately to the gross fluxes, not for the net difference (i.e. *GPP* – *RESP*) between them. Large prior uncertainties may allow more freedom for the biases to move. The use of such priors needs dense observation network in order to find an optimal solution. Smaller prior uncertainties may lead biases to get stuck in a wrong solution. The choice of prior uncertainties is arbitrary. Ocean biases are allowed very minor changes. Therefore the results can be well interpreted only for well-observed land regions and cannot make quantitative flux estimates for other land regions or the oceans.

In MLEF, for each subsequent cycle, prior and the covariance of the biases have to be defined. That is, we define the center value for the estimate and its variability by an analysis covariance matrix from the previous cycle to condition the distribution from which candidate **β**s are selected at each grid cell for each ensemble member of the next cycle. In MLEF, the average of posterior from previous cycle and prescribed values from the initial cycle is considered as the prior. Hence, according to our assumption, the average of the previous analysis state and the forecast state in the initial cycle becomes the prior state for the next cycle. Similarly, the uncertainty of the biases, which is the covariance matrix of the biases also needed to be defined. In the case of unreasonably smaller values of the error covariance, the perturbations used to generate each ensemble member would become very small and the **β**s could converge to incorrect values. To avoid this problem, the covariance matrix is "inflated" in each new cycle. In MLEF, covariance inflation was done by applying a higher weight (= 0.9) for the initial covariance as given in Equation (2).

$$\text{Prior covariance for the current cycle} = (0.1 \times \text{analyzed covariance from previous cycle}) + (0.9 \times \text{initial covariance}) \quad (2)$$

In the case of an under-determined problem, an optimal solution can only be reached when the ensemble size is very large. However, larger ensemble sizes involve high computational cost. Hence smoothing and localization schemes have been applied to alleviate the problems of sparse sampling. Covariance smoothing is introduced only in the first data assimilation cycle according to an exponential decay function (Lokupitiya et al., 2008; Michalak et al, 2004; Peters et al., 2005; Rödenbeck et al., 2003). In this study, we chose to smooth the prescribed covariance in the initial assimilation cycle with an e-folding length of 800 km over the land points and 1600 km over the ocean points.

Subsequently, we introduced a localization scheme, which is sensitive to dynamical changes in the posterior (analysis) and prior (forecast) uncertainties (Lokupitiya et al., 2008; Zupanski et al., 2007). To define the "distance" for covariance localization, we employed the ratio *r* between the prior (σ_{Prior}) and the posterior ($\sigma_{Posterior}$) uncertainty of the current cycle defined as $r = \sigma_{Prior} / \sigma_{Posterior}$. The greater values of the ratio represent the areas with the greater influence from the observations. We set the influence regions based on the distribution of the ratio r. We restricted adjustments to model biases to the 40% of land points and 10% of ocean points best constrained by the observations, based on the upper tail values of the ratio probability distribution. This choice selects the densely observed regions. Only these selected regions are allowed to change from the prior mean. The forward model is run with the revised biases to produce the 3-D CO_2 fields for the next assimilation cycle. CarbonTracker uses a localization scheme based on the correlation coefficient between the parameter deviations and the observation deviations. Cut-off values are selected according to the two-tailed student's *T*-test, at 95% significance level (Peters et al., 2007).

2.3.4 Ensemble size

In order to determine the adequate ensemble size, Lokupitiya et al. (2008) and Zupanski et al. (2007) used an information measure referred to as Degrees of Freedom for Signal (DFS). Given the number of observations and the ensemble size, DFS being a positive integer indicates whether the selected ensemble size was appropriate (Lokupitiya et al., 2008). In this study, we used 90 ensemble members for the data assimilation.

2.4 CO_2 observation network used for data assimilation

We assimilated flasks and continuous observations obtained from the existing observation networks (see Figure 1 and Table 1) and CONTRIAL CO_2 measurements (see Figure 9) for the years from 2009 to 2011. Flask and continuous observations are collected near the surface. The temporal variation in the vertical structure is still relatively limited through these observations. This may result an incomplete view of the three-dimensional temporal variation of atmospheric CO_2. However, research aircraft measurements can provide vertical and horizontal distributions of CO_2 with sufficient precision to validate transport models, as well as being useful in providing an increased level of constraint in carbon flux estimates by inverse modelling (Sawa et al., 2012)..

Table 1. Continuous and Flask CO_2 measurement sites used in this study

Site Name	Latitude	Longitude	Elevation	Observation error		
				2009	2010	2011
Air samples collected in glass flasks						
Alert, Nunavut, Canada (ALT)	82.45	-62.51	0	3.39	3.18	5.16
Amsterdam Island, France (AMS)	-37.95	77.53	0	2.00	2.00	2.00
Ascension Island, United Kingdom (ASC)	-7.97	-14.40	0	2.89	2.35	2.25
Assekrem, Algeria (ASK)	23.26	5.63	2710	2.24	2.55	2.87
St. Croix, Virgin Islands, United States (AVI)	17.75	-64.75	0	2.00	2.00	2.00
Terceira Island, Azores, Portugal (AZR)	38.77	-27.38	0	1.85	1.49	3.87
Baltic Sea, Poland (BAL)	55.35	17.22	0	9.64	9.85	6.66
Baring Head Station, New Zealand (BHD)	-41.41	174.87	0	2.57	2.54	2.51
Bukit Kototabang, Indonesia (BKT)	-0.20	100.32	0	6.28	6.27	4.36
St. Davids Head, Bermuda, United Kingdom (BME)	32.37	-64.65	0	4.51	2.28	2.00
Tudor Hill, Bermuda, United Kingdom (BMW)	32.26	-64.88	0	3.42	3.63	3.99
Barrow Atmospheric Baseline Observatory, United States (BRW)	71.32	-156.61	0	4.51	4.43	5.88
Black Sea, Constanta, Romania (BSC)	44.18	28.66	0	15.87	15.39	15.85
Cold Bay, Alaska, United States (CBA)	55.21	-162.72	0	3.39	3.73	5.28
Cape Grim, Tasmania, Australia (CGO)	-40.68	144.69	0	2.86	2.83	2.66
Christmas Island, Republic of Kiribati (CHR)	1.70	-157.15	0	1.57	1.52	1.72
Cape Meares, Oregon, United States (CMO)	45.48	-123.97	0	2.00	2.00	2.00
Crozet Island, France (CRZ)	-46.43	51.85	0	2.94	2.83	3.34
Easter Island, Chile (EIC)	-27.15	-109.45	0	2.79	2.78	2.69
Mariana Islands,Guam (GMI)	13.39	144.66	0	1.72	2.11	2.22
Dwejra Point, Gozo, Malta (GOZ)	36.05	14.89	0	2.00	2.00	2.00
Halley Station, Antarctica, United Kingdom (HBA)	-75.61	-26.21	0	8.83	8.61	9.30
Hohenpeissenberg, Germany (HPB)	47.80	11.02	0	9.47	10.00	10.06
Hegyhatsal, Hungary (HUN)	46.95	16.65	0	11.31	10.12	13.30
Storhofdi, Vestmannaeyjar, Iceland (ICE)	63.40	-20.29	0	3.04	2.00	2.00
Izana, Tenerife, Canary Islands, Spain (IZO)	28.30	-16.48	2373	2.20	2.38	3.03
Kaashidhoo, Republic of Maldives (KCO)	4.97	73.47	0	2.00	2.00	2.00
Key Biscayne, Florida, United States (KEY)	25.67	-80.20	0	2.95	3.13	3.22
Cape Kumukahi, Hawaii, United States (KUM)	19.52	-154.82	0	2.16	2.65	3.39
Sary Taukum, Kazakhstan (KZD)	44.08	76.87	0	7.80	2.00	2.00
Plateau Assy, Kazakhstan (KZM)	43.25	77.88	2519	5.36	2.00	2.00
Lampedusa, Italy (LMP)	35.52	12.62	0	3.66	3.54	4.46
Mace Head, County Galway, Ireland (MHD)	53.33	-9.90	0	3.74	3.91	4.63
Sand Island, Midway, United States (MID)	28.21	-177.38	0	2.57	3.02	4.12
Mt. Kenya, Kenya (MKN)	-0.06	37.30	3644	3.12	3.63	2.28

Table 1. (Continued)						
Mauna Loa, Hawaii, United States (MLO)	19.54	-155.58	3397	1.91	2.37	2.26
Niwot Ridge, Colorado, United States (NWR)	40.05	-105.58	3523	3.40	3.73	4.51
Olympic Peninsula, Washington, United States (OPW)	48.30	-124.63	0	2.00	2.00	2.00
Pallas-Sammaltunturi, GAW Station, Finland (PAL)	67.97	24.12	0	8.04	6.46	6.94
Palmer Station, Antarctica, United States (PSA)	-64.92	-64.00	0	7.35	7.61	7.69
Point Arena, California, United States (PTA)	38.95	-123.73	0	5.91	6.37	7.75
Ragged Point, Barbados (RPB)	13.17	-59.43	0	2.20	2.49	2.97
Mahe Island, Seychelles (SEY)	-4.68	55.53	0	1.68	1.31	1.74
Southern Great Plains, Oklahoma, United States (SGP)	36.80	-97.50	0	13.82	10.24	8.68
Shemya Island, Alaska, United States (SHM)	52.72	174.10	0	3.53	3.73	6.07
Tutuila, American Samoa (SMO)	-14.25	-170.56	0	1.31	0.88	1.10
South Pole, Antarctica, United States (SPO)	-89.98	-24.80	0	10.96	12.23	12.31
Ocean Station Charlie, United States (STC)	54.00	-35.00	0	2.00	2.00	2.00
Ocean Station M, Norway (STM)	66.00	2.00	0	4.63	2.00	2.00
Summit, Greenland (SUM)	72.60	-38.42	3209	2.93	2.79	5.01
Syowa Station, Antarctica, Japan (SYO)	-69.00	39.58	0	4.04	3.87	3.91
Tae-ahn Peninsula, Republic of Korea (TAP)	36.73	126.13	0	5.82	5.94	6.69
Trinidad Head, California, United States (THD)	41.05	-124.15	0	4.68	5.12	6.67
Wendover, Utah, United States (UTA)	39.90	-113.72	0	4.44	4.49	3.70
Ulaan Uul, Mongolia (UUM)	44.45	111.10	0	3.61	3.54	5.48
Weizmann Institute of Science at the Arava Institute, Ketura, Israel (WIS)	30.86	34.78	0	3.60	3.41	5.26
Mt. Waliguan, Peoples Republic of China (WLG)	36.29	100.90	0	3.31	3.28	3.87
Ny-Alesund, Svalbard, Norway and Sweden (ZEP)	78.90	11.89	0	3.68	3.43	5.44
Continuous In-situ CO_2 analyzer from Towers.						
Argyle, Maine, United States (AMT)	45.03	-68.68	107	10.48	9.59	9.25
lef011 - Park Falls, Wisconsin, United States (LEF)	45.94	-90.27	11	9.36	2.00	2.00
lef030	45.94	-90.27	30	11.10	8.08	10.30
lef076	45.94	-90.27	76	7.59	2.00	2.00
lef122	45.94	-90.27	122	8.17	6.89	9.43
lef244	45.94	-90.27	244	4.90	2.00	2.00
lef396	45.94	-90.27	396	6.93	6.45	8.89
wkt009 - Moody, Texas, United States (WKT)	31.32	-97.33	9	2.00	2.00	2.00
wkt030	31.32	-97.33	30	8.15	7.90	6.77
wkt061	31.32	-97.33	61	2.00	2.00	2.00
wkt122	31.32	-97.33	122	6.77	6.90	6.35
wkt244	31.32	-97.33	244	2.00	2.00	2.00
wkt457	31.32	-97.33	457	4.96	5.56	5.39
In-situ co2 hourly averages						
Mauna Loa, Hawaii, United States (MLO)	19.54	-155.58	3397	1.97	2.37	2.23
Barrow Atmospheric Baseline Observatory, United States (BRW)	71.32	-156.61	11	4.49	4.17	5.95
Anmyeon-do, Republic of Korea (AMY)	36.54	126.33	46	8.50	8.19	8.01
Candle Lake, Canada (CDL)	53.99	-105.12	600	5.34	5.55	2.00
Chibougamau, Canada (CHM)	49.69	-74.34	393	4.75	4.78	6.37
Cape Point, South Africa (CPT)	-34.35	18.49	230	2.96	2.72	2.86
Fraserdale, Canada (FSD)	49.86	-81.57	210	5.96	6.00	7.19
Izaña (Tenerife), Spain (IZO)	28.31	-16.50	2373	2.18	2.36	3.13
Mace Head, Ireland (MHD)	53.33	-9.90	5	5.43	5.43	6.48
Neuglobsow, Germany (NGL)	53.14	13.03	62	14.46	15.73	16.62
Ryori, Japan (RYO)	39.03	141.82	260	7.82	8.92	7.09
Schauinsland, Germany (SSL)	47.90	7.92	1205	6.94	7.79	6.74
Yonagunijima, Japan (YON)	24.47	123.01	30	4.73	5.33	5.46
Zeppelin Mountain (Ny Ålesund), Norway (ZEP)	78.91	11.89	475	3.92	3.49	5.20

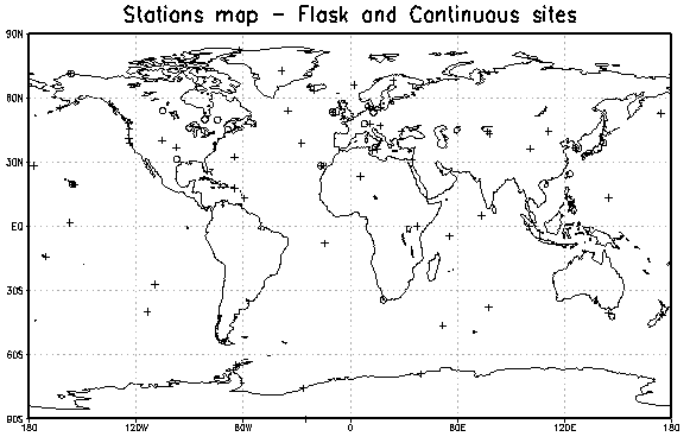

Figure 1. A map of the continuous and flask stations used in this study except CONTRAIL. Open circles depict continuous measurement sites (see Table 1). Crosses identify flask-sampling locations that are part of the NOAA-ESRL network (GLOBALVIEW-CO2).

2.4.1 In-situ CO_2 measurements

Flask and in-situ CO_2 observations used in this study were taken mainly from two observation networks, GLOBALVIEW-CO_2 and WDCGG (World Data Centre for Greenhouse Gases). GLOBALVIEW-CO_2 is a product of the Corporative Atmospheric Data Integration Project coordinated and maintained by NOAA ESRL (National Oceanic and Atmospheric Administration, Earth System Research Laboratory). NOAA provides high-quality CO_2 measurements collected from multiple institutions (https://www.esrl.noaa.gov/). WDCGG is a World Data Centre (WDC) operated by the Japan Meteorological Agency (JMA) under the Global Atmosphere Watch (GAW) programme of the World Meteorological Organization (WMO). It collects, archives and distributes data provided by contributors on greenhouse gases such as CO_2, CH_4, CFC, N_2O and related gases such as CO in the atmosphere and elsewhere (https://gaw.kishou.go.jp/). In this study, the observation vector consists of 58 surface flask observations sites collected on weekly basis and 27 continuous sites that are measuring in-situ at different vertical levels on the hourly basis in addition to the CONTRAIL data.

In this study, the diurnal cycle at continuous sites were filtered according to the local meteorology. Low-elevation sites (LEF, WKT, MHD) were used during mid-day only (11 to 16 hours local time) because well-developed boundary-layer mixing is better simulated in the transport model than stable nocturnal conditions or morning and evening transitions. Mountaintop sites (MLO, IZO and SSL) were used at night (0-4 hours local time), because subsiding mid-tropospheric air at night better represents model conditions than upslope conditions during the day. Impact from each observation site varies according to how well transport model captures the observations at the site. These differences in the transport represent the diagonal elements of the observation error covariance matrix.

We computed average model-data mismatch error at each site as the observation error, by running transport model (PCTM) separately for the years 2009-2011 (Table 1). Observation errors at the multi-level observation stations such as LEF and WKT vary according to the height of the measurement levels. When compared with other continuous sites, station NGL shows the highest observation error for each year (Figure 2). Errors at the flask stations vary between

the minimum and the maximum values of 1.31 ppm - 15.87 ppm, 0.88 ppm – 15.39 ppm and 1.1 ppm – 15.85 ppm for the years 2009, 2010, and 2011, respectively (Figure 3).

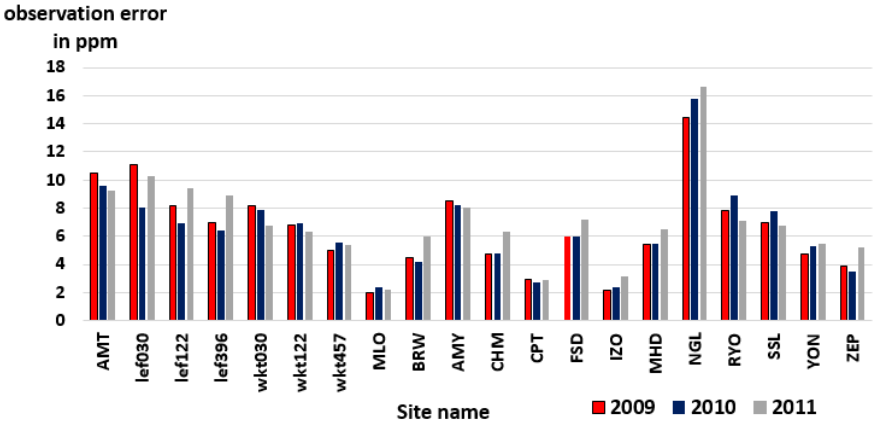

Figure 2. Variation of the observation errors for Continuous stations for the years 2009-2011.

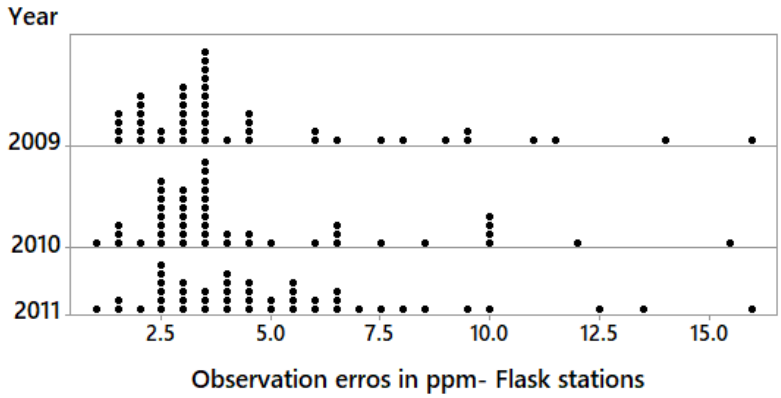

Figure 3. Variation of the observation errors for Flask stations for the years 2009-2011.

2.4.2 CONTRAIL CO_2 measurements

In order to achieve a better global view of the three-dimensional variations in CO_2 measurements, CONTRAIL measurements were also used in this study. Five "JAL" air planes on regular commercial service measure CO_2 continuously during each flight. In addition to the vertical profiles of CO_2 during ascent and descent, horizontal measurements are obtained along the flight path. The aircraft measurements cover a substantial geographical region, with a wide longitudinal coverage (0°E–115°W) in mid-latitudes to high latitudes in Northern Hemisphere. The CONTRAIL observation extends in the north-south direction, along the various JAL flights between Japan, Australia and Southeast Asia. This observation provides regional vertical/upper atmospheric CO_2 data over extensive areas in the Eurasian continent, Tropical region and the Southern Hemisphere where the number of surface stations are limited (http://www.cger.nies.go.jp/contrail/index.html access: 01 August 2019). The flights cover the area 30S- 50N and 60-160E (Figure 9). Model data mismatch errors for CONTRAIL locations are shown in Figure 4.

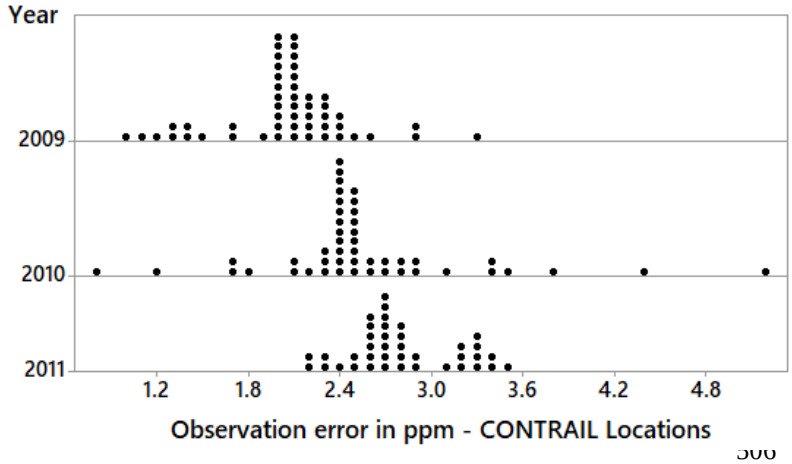

Figure 4. Variation of the observation errors for CONTRAIL locations for the years 2009-2011.

2.5 Model comparison with Carbon Tracker

We compared our results with CarbonTracker (CT2017), another ensemble-based data assimilation system (Peters et al., 2005, 2007, CT2017 release at https://www.esrl.noaa.gov/gmd/ccgg/carbontracker/CT2017/), which has been developed based on the fixed-lag Kalman smoother (Bruhwiler et al., 2005) and ensemble square root filter (Whitaker & Hamill, 2002). CT2017 uses multiple in-situ observation networks and prior models to optimize weekly fluxes over 126 land "ecoregions" and 30 ocean regions (Peters et al., 2007; https://www.esrl.noaa.gov/gmd/ccgg/carbontracker/CT2017_doc.php, last acces:16 August 2019). CT2017 uses TM5 transport model which connects the surface fluxes to atmospheric CO_2 mole fractions. The model uses measurements of air samples collected at 254 sites around the world by 55 laboratories and assimilates hourly average CO_2 concentrations. CT2017 uses two biosphere models, which provide first-guess terrestrial fluxes. CASA (Carnegie-Ames Stanford Approach) calculates global carbon fluxes using input from weather models to drive biophysical processes, and satellite observed Normalized Difference Vegetation Index (NDVI) to track plant phenology. Global Fire Emissions Database Version 4.1 (GFEDv4) is used as one of the fire modules to estimate biomass burning, and climatological estimates of CO_2 partial pressure in surface waters (pCO_2) from Takahashi et al. (2002) is used as the first-guess of air-sea flux. In CT2017, observed-minus-forecasted mole fraction that exceeds 3 times the prescribed model-data mismatch has been considered as an indicator that the modeling framework fails. The scaling factors λ are estimated independently for each week and optimization region using a moving overlapping assimilation window. CarbonTracker solves for fluxes by considering multiplicative scaling factors (biases) in NEE and air-sea gas exchange. CarbonTracker uses 150 ensemble members in their flux estimation.

3 Results and Discussion

This section is organized as three parts: performance of the transport model in simulating the CO_2 concentrations, characteristics of the optimized CO_2 fluxes (biosphere and ocean) using MLEF for the years 2009-2011 and comparison of the MLEF results with other studies mainly over the North America, Europe, Asia and Australia.

3.1 Evaluation of the transport model simulation

We checked the performance of PCTM model by comparing model simulated CO_2 with the observed CO_2 at observation network used in this study which consists of flask, continuous and CONTRAIL measurements. After a three-year spin-up from years 2006-2008, CO_2 at observation stations were sampled for years 2009-2011. For the comparison with actual CO_2 measurements, a global constant off-set values have been added at each observation station. Figure 5 shows a comparison between PCTM simulated CO_2 and the actual CO_2 measurements at the continuous sites AMT, BRW and FSD for the years from 2009 to 2011.

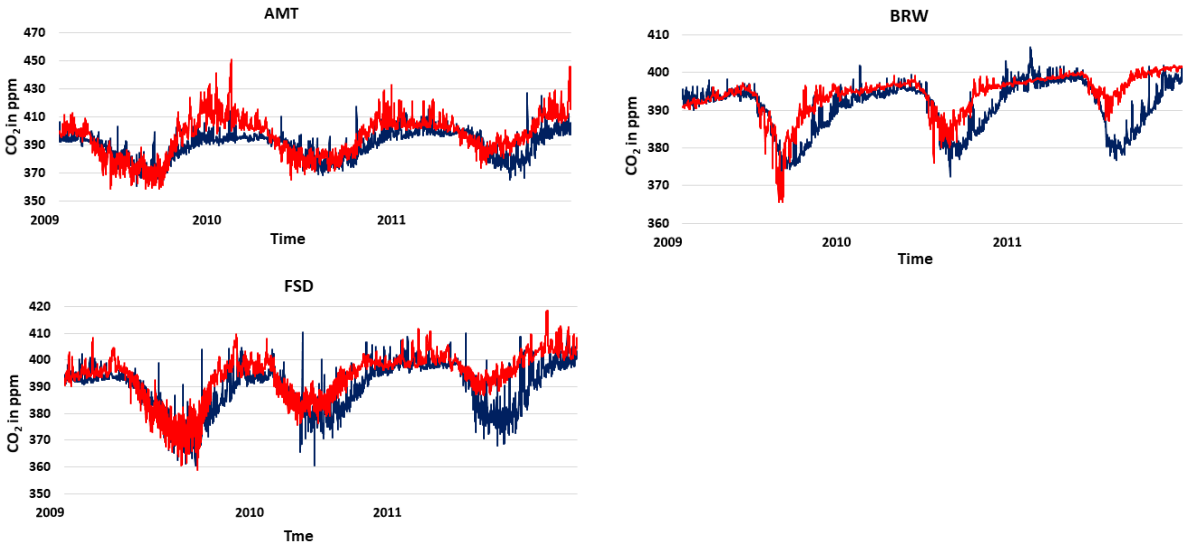

Figure 5. Observed hourly CO_2 concentrations (in blue) and simulated CO_2 (in red) from PCTM for years from 2009 – 2011 at stations FSD (Fraserdale, Canada), AMT (Argyle, Maine, United States) and BRW (Barrow Atmospheric Baseline Observatory, United States).

Observation error for each observation site is calculated by averaging the difference between observed values (actual CO_2) and the PCTM simulated CO_2 values throughout the year. Observation errors for the flask and continuous sites for the years 2009-2011 are given in Table 1. Figures 2 and 3 summarize the variation of the observation errors (actual – simulated) from 2009-2011 for each continuous site and flask station. According to the above results, site "NGL" in Germany shows the highest observation error in each year. When compared with all other sites, "MLO", "CPT", "IZO" and "ZEP" show relatively low observation errors. For the flask stations, observation errors vary from 0.88 ppm to 16.0 ppm. Variation of the observation errors for the CONTRAIL locations are shown in Figure 4. Observation errors of CONTRAIL locations show considerably small values than flask and continuous stations. The average and uncertainty of the observation errors are 2.04 ± 0.43 ppm, 2.56 ± 0.71 ppm and 2.81 ± 0.36 ppm for the years 2009, 2010, and 2011, respectively. According to above results, simulated CO_2 using PCTM shows good agreement with the flask and continuous measurements as well as the CONTRAIL measurements.

3.2 Forward model comparisons

We used forward model comparisons to test the quality of the data assimilation. Figure 6 shows observed daily mean CO_2 concentrations along with the daily mean recovered and prior CO_2 concentrations obtained from optimized (posterior) fluxes and prior fluxes at North American stations (Argyle, Maine, United States (AMT), Barrow Atmospheric Baseline Observatory, United States (BRW), Chibougamau, Canada (CHM)) and several stations in Asian region (Ryori, Japan (RYO), Anmyeon-do, Republic of Korea (AMY) and Yonagunijima, Japan (YON)) for the years 2009 to 2011.

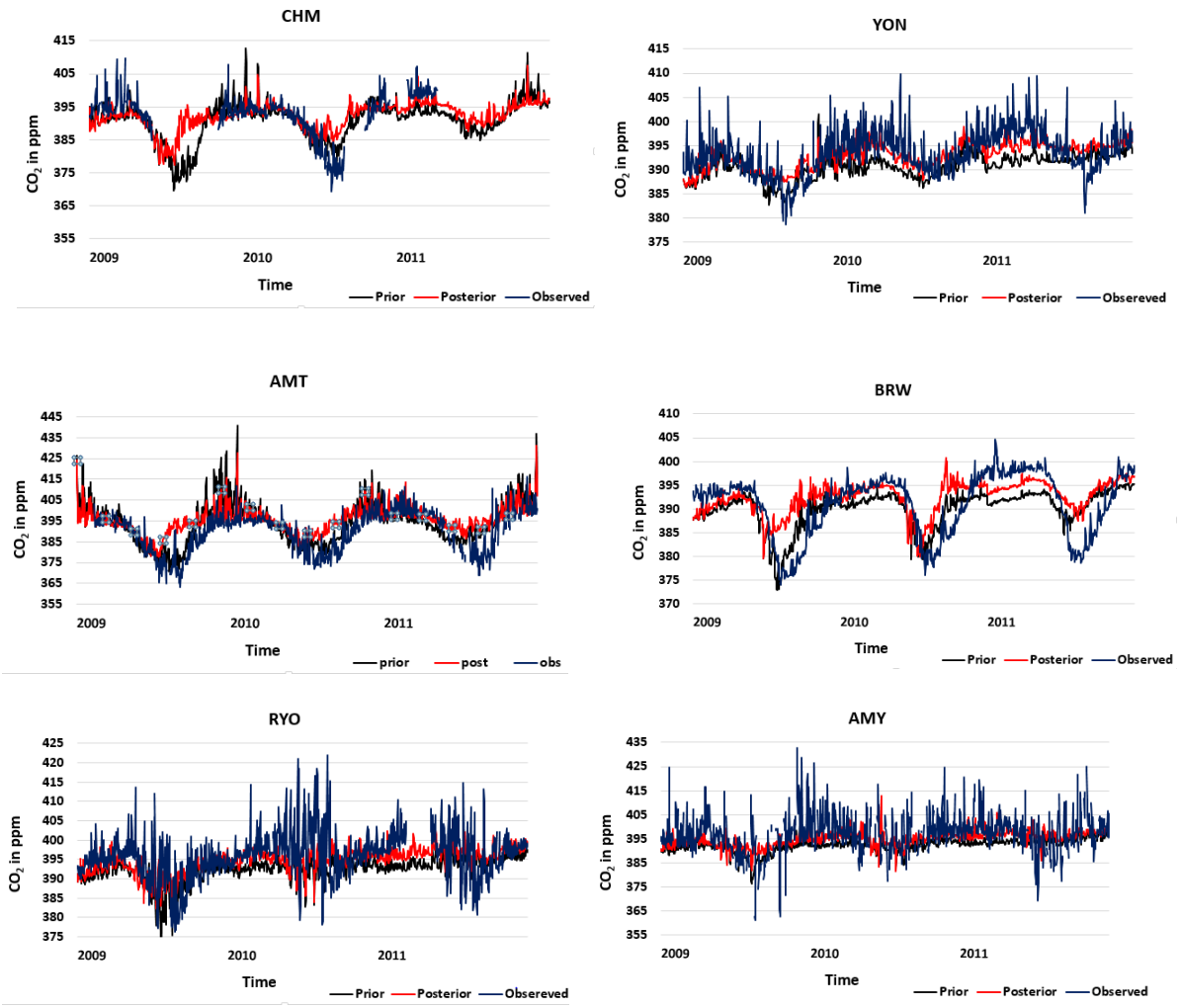

Figure 6. Daily time series plots of CO_2 concentrations from posterior fluxes (in red) and prior fluxes (in black) compared to observations (in blue) for years 2009 – 2011 at Yonagunijima, Japan (YON), Ryori, Japan (RYO), Anmyeon-do, Republic of Korea (AMY), Argyle, Maine, United States (AMT), Chibougamau, Canada (CHM) and Anmyeon-do, Republic of Korea (AMY)

641 **Table 2.** Root Mean Square Error (RMSE) with respect to the prior and the posterior at
642 continuous sites for 2009 to 2011 Units: parts per million by volume (ppmv)
643

Station	Latitude (deg)	Longitude (deg)	Elevation (m)	2009			2010			2011		
				RMSE Prior	RMSE Posterior	Difference	RMSE Prior	RMSE Posterior	Difference	RMSE Prior	RMSE Posterior	Difference
AMT	45.03	-68.68	107	9.18	9.82	-0.64	7.66	8.34	-0.68	8.69	9.02	-0.33
LEF011	45.94	-90.27	11	5.93	4.28	1.65		-	*	-	-	-
LEF030	45.94	-90.27	30	8.61	11.8	-3.19	7.16	9.19	-2.03	9.73	11.53	-1.80
LEF076	45.94	-90.27	76	5.40	3.92	1.48	-	-	-	-	-	-
LEF122	45.94	-90.27	122	7.89	10.93	-3.04	6.78	8.63	-1.85	9.34	10.89	-1.55
LEF244	45.94	-90.27	244	4.51	3.49	1.02	-	-	-	-	-	-
LEF396	45.94	-90.27	396	7.71	10.59	-2.88	6.49	8.01	-1.52	8.93	10.10	-1.17
WKT009	31.32	-97.33	9	-	-	-	-	-	-	-	-	-
WKT030	31.32	-97.33	30	4.99	5.52	-0.53	5.94	6.31	-0.37	5.85	5.37	0.48
WKT061	31.32	-97.33	61	-	-	-	-	-	-	-	-	-
WKT122	31.32	-97.33	122	4.75	5.19	-0.44	5.74	5.91	-0.17	5.77	5.18	0.59
WKT244	31.32	-97.33	244	-	-	-	-	-	-	-	-	-
WKT457	31.32	-97.33	457	4.07	4.61	-0.54	5.21	5.41	-0.20	5.15	4.63	0.52
MLO	19.54	-155.58	3397	1.56	2.27	-0.71	2.33	2.63	-0.30	2.22	2.74	-0.52
BRW	71.32	-156.61	11	4.12	6.37	-2.25	3.95	5.10	-1.15	5.92	5.37	0.55
AMY	36.54	126.33	46	10.02	9.33	0.69	9.48	8.39	1.09	8.80	7.91	0.89
CDL	53.99	-105.12	600	4.96	6.53	-1.57	5.42	5.68	-0.26	-	-	-
CHM	49.69	-74.34	393	4.59	4.57	0.02	4.58	5.44	-0.86	6.17	4.08	2.09
CPT	-34.55	18.49	230	3.07	3.72	-0.65	2.64	4.56	-1.92	2.74	4.81	-2.07
FSD	49.86	-81.57	210	5.19	8.66	-3.47	5.76	7.43	-1.67	7.31	7.56	-0.25
IZO	28.31	-16.50	2373	1.98	3.12	-1.14	2.34	3.53	-1.19	3.11	3.44	-0.33
MHD	53.33	-9.90	5	-	-	-	5.11	5.78	-0.67	6.34	6.70	-0.36
NGL	53.14	15.03	62	11.89	15.73	-3.84	14.94	14.53	0.41	15.98	17.71	-1.73
RYO	39.03	141.82	260	6.03	5.45	0.58	8.41	7.23	1.18	6.75	5.86	0.89
SSL	47.90	7.92	1205	5.74	6.05	-0.31	7.83	7.88	-0.05	6.34	6.03	0.31
YON	24.47	123.01	30	3.98	3.60	0.38	5.15	3.61	1.54	5.35	3.98	1.37
ZEP	78.91	11.89	475	4.14	5.99	-1.85	3.45	4.29	-0.84	5.19	4.59	0.60

644
645
646 Recovered CO_2 from posterior fluxes for these sites show good agreement with the actual CO_2
647 concentrations. Table 2 summarizes the Root Mean Square Errors (RMSE) with respect to the
648 prior and the posterior for all the continuous sites used for the inversion. Among the prior
649 RMSE for continuous stations, station "NGL" in Europe shows the largest average prior RMSE
650 with 13.15 ± 1.29 ppm per year. This indicates a poor representation of the prior fluxes and/or
651 deficiencies in the transport in that station. Very large observation errors in the station "NGL"
652 under Section 3.1 confirms this result. Inclusion of these stations may have a significant impact
653 on the overall solution. Posterior CO_2 concentrations at Asian stations like "RYO", "YON"
654 and "AMY", show better agreement with observed CO_2 concentrations. This may be due to the
655 effect of the CONTRAIL CO_2 measurements in the observation vector (Figure 6). Patra et al.
656 (2008) has analyzed the synoptic-scale variability in the model simulations and observations
657 for several approaches. This study concluded that the differences of the transport model
658 performances depend on the horizontal and vertical characteristics of the sampling locations
659 corresponding to each model and those are fairly independent of the size of the observed
660 variability at the sites. In this study, it was identified that site "LEF", which records CO_2 at
661 several vertical layers up to about 400m, has considerably overestimated the magnitude of
662 synoptic variations at lower levels for the period of 2002-2003. Correlations between observed
663 and modeled CO_2 time series were also calculated and it was found that the correlation
664 coefficient is greater than 0.3 at most stations.
665
666
667
668
669
670

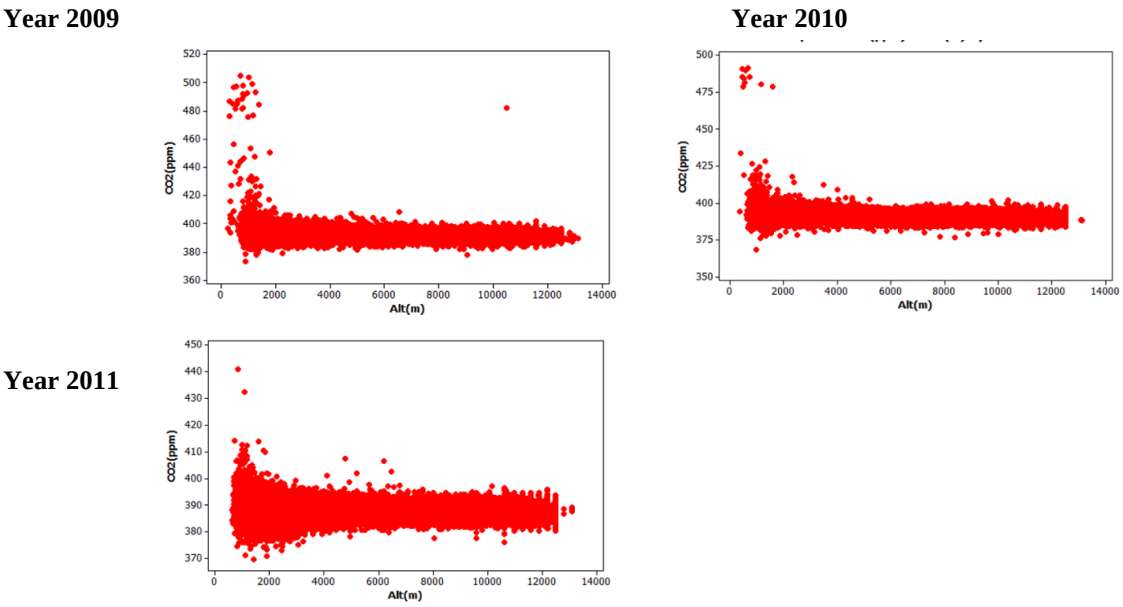

Figure 7. Variation of CONTAIL CO_2 observations with relevant altitude (m).

Figure 7 shows the variation of the observed CONTRAIL CO_2 values with flight altitude. CONTRAIL CO_2 shows a higher variability at lower altitudes for each year. Niwa et al. (2012) also used four vertical bins as 575-625, 475-525, 375-425, 225-275 hPa because some measurements at lower altitudes (in boundary layer) are polluted by local polluted air from major cities where airports are commonly situated. They did not use the measurements below 625 hPa in order to get more accurate estimates. In this study, CONTRAIL CO_2 locations in between the altitudes from 4000m to 11000m are used for the data assimilation. The performance of MLEF method on estimating CONTRAIL aircraft data were also measured by calculating the RMSE values considering estimated posterior CO_2 and observed CO_2 values under four different height levels (i.e. 4000-5201, 5201-7074, 7074-8322 and 8322-11000 m). The RMSE values are given in Table 3.

Table 3. Root Mean Square Error (RMSE) with respect to the posterior CONTRAIL CO_2 measurements for 2009 to 2011 Units: parts per million by volume (ppmv)

		Year 2009	
Altitude in meters	**Pressure level**	**Number of observations**	**RMSE (ppm)**
2912 – 5202 m	**350 - 625 hPa**	2292	2.62
5202 – 7075 m	**625 - 850 hPa**	3869	2.39
7075 – 8323 m	**850 - 1000 hPa**	2696	2.23
8323 – 11000 m	**1000 - 1325 hPa**	9434	2.31

		Year 2010	
Altitude in meters	**Pressure level**	**Number of observations**	**RMSE (ppm)**
2912 – 5202 m	**350 - 625 hPa**	2128	3.11
5202 – 7075 m	**625 - 850 hPa**	3629	3.02
7075 – 8323 m	**850 - 1000 hPa**	2492	3.04
8323 – 11000 m	**1000 - 1325 hPa**	9668	3.14

		Yesr 2011	
Altitude in meters	**Pressure level**	**Number of observations**	**RMSE (ppm)**
2912 – 5202 m	**350 - 625 hPa**	2034	3.76
5202 – 7075 m	**625 - 850 hPa**	3359	3.74
7075 – 8323 m	**850 - 1000 hPa**	2313	3.64
8323 – 11000 m	**1000 - 1325 hPa**	8984	3.32

According to Table 3, the locations in low altitudes show relatively high RMSE values than other levels. Figure 8 shows the difference between the observed and predicted CO_2 concentrations for the CONTRAIL locations under the selected altitude levels from 2009-2011. The errors are symmetrically distributed for each height level for the years 2009 and 2010 except for year 2011.

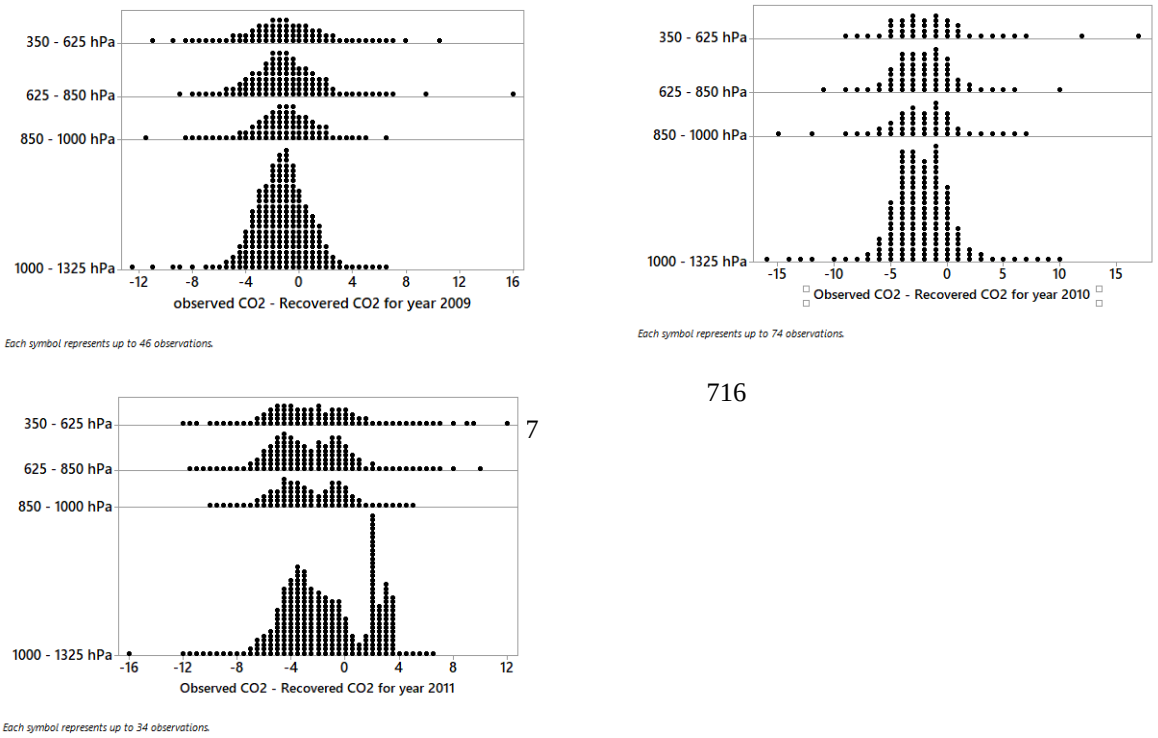

716

7

Figure 8. Distribution of the difference between observed CO_2 and recovered CO_2 under four vertical bins for years 2009 to 2011.

3.3 Chi-square test statistic

The quality of the data assimilation process was tested using several measures. Another measure is the χ^2 statistic which evaluates the innovation (observed minus forecast observation) covariance matrix (Zupanski, 2005). Under the Gaussian assumption and for a linear observation operator, this statistic should be equal to one for statistical consistency, which suggests that the posterior uncertainty is consistent with the quality of the fit to the data. In reality, however, it is not exactly equal to one due to statistically small samples (i.e. relatively few observations per cycle). In this study, average χ^2 for the three years approximately equals 0.46 ± 0.12, 0.41 ± 0.08 and 0.42 ± 0.17 which indicates that the errors are moderately consistent.

3.4 Uncertainty reduction

Figure 9 shows the average uncertainty reduction with respect to the prescribed prior uncertainty at the initial cycle. The uncertainty reduction is calculated as a percentage value as given in equation (3).

$$\text{Uncertainty reduction} = \frac{\sigma_{prior} - \sigma_{posterior}}{\sigma_{prior}} \times 100, \quad (3)$$

where σ_{prior} and $\sigma_{posterior}$ are the prior uncertainty at the initial cycle and the posterior uncertainty, respectively.

(a) year 2009

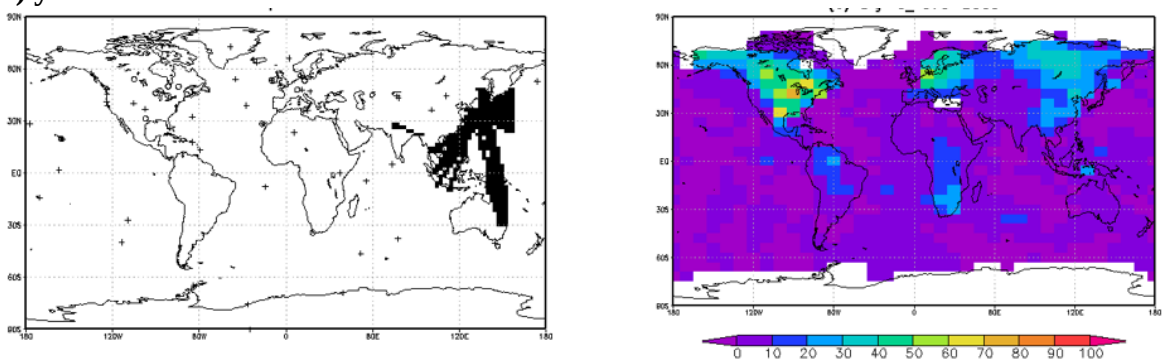

(b) year 2010

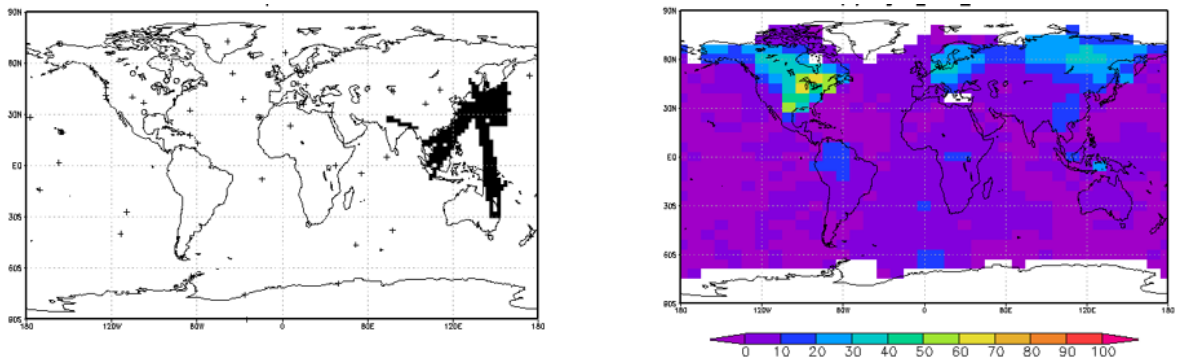

(c) year 2011

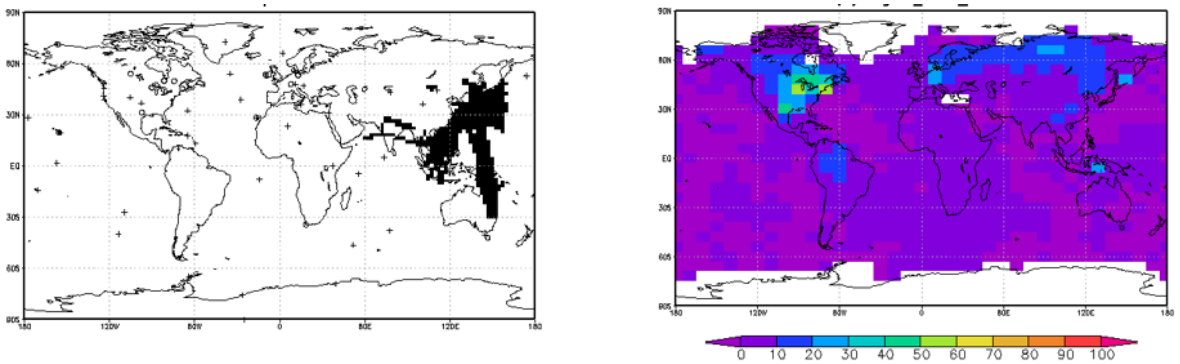

Figure 9. Stations map with CONTRAIL locations and mean annual percentage uncertainty reduction for the years (a) 2009, (b) 2010 and (c) 2011.

According to Figures 1 and 9 the densely observed North American region show a good constraint (about 60-80% uncertainty reduction) on flux estimates for 2009 and 60-70% reduction for 2010 and 2011. European region shows 50-60% uncertainty reduction for 2009 and 40-50% reduction for 2010 and 2011. The East Asia and Southeast Asia region show about 50 to 60 percent uncertainty reduction for 2009 and 30-50% reduction for 2010 and 2011. The lower uncertainty reduction in Asian region for the years 2010 and 2011 may be due to the effect of relatively high observation errors of CONTRAIL measurements in year 2010 and 2011 than the year 2009 (Figure 8). The recovery of the ocean fluxes is poor due to the weak signal from the ocean flux that is observed at the stations. Ocean fluxes are an order of magnitude weaker than those on land, so the land fluxes dominate the signal (especially due to the large number of observations from continuous stations) at atmospheric observation sites on the 8-week time scale. Ocean biases are given less prior uncertainty compared to the land, which limits the uncertainty reduction in ocean fluxes. Note that we do not claim that the ocean fluxes given by the priors are correct, rather that the atmospheric observations provide insufficient constraint for our assimilation scheme to provide improved estimates at the grid scale.

In each assimilation cycle, grid boxes that are strongly influenced by the observation network are selected according to the localization scheme and allowed to change $\boldsymbol{\beta}$ from the prior. Hence the posterior fluxes from sparsely observed areas are mainly dominated by the priors. Currently, grid boxes, which are selected according to the localization scheme, are equally weighted.

The posterior land flux uncertainties have contributions from the variances of the GPP and respiration biases and their cross-covariance (see Equation 4, Lokupitiya et al., 2008).

$$Var(F) = RESP^2 Var(\beta_{RESP}) + GPP^2 Var(\beta_{GPP}) - 2 \times RESP \times GPP \times Cov(\beta_{RESP}, \beta_{GPP}) \quad (4)$$

We have assumed that the observation error covariance matrix ($\boldsymbol{R}$) is diagonal, which means that the observation stations are far enough from each other so that the correlations among their errors are negligible (off-diagonal elements of $\boldsymbol{R}$ are zero). Inclusion of these off-diagonal covariance terms in the observation errors would produce a result that was closer to the prior (neutral carbon balance). In this study, we split the net contribution into two component fluxes, GPP and respiration. This method allows the recovery of flux patterns with a loose prior and potentially facilitates identification of each component's contribution to the NEE, which can help explain the underlying biogeochemical processes.

3.5 Comparison of optimized carbon fluxes with CT2017 fluxes

Fluxes optimized by MLEF are compared with the CT2017 (The version of the CarbonTraker used in this study is based on the CarbonTracker 2017 release) fluxes for the globe. The stations maps of CO_2 observation vector under the two inversion methods, MLEF and CT2017 for the period 2009-2011 are given in Figure 10. In Figure 11, left panel and the right panel show the posterior land fluxes (NEE) obtained from MLEF and CarbonTracker method (CT2017) for the years 2009-2011 respectively. CatbonTracker flux maps were created using the downloaded optimized fluxes in monthly averages from NOAA site (http://aftp.cmdl.noaa.gov/). The regions such as Tropical Asia, Temperate Eurasia, Australia, Europe, Boreal North America and Temperate North America were considered for the comparison due to considerable amount of observations over the region. TransCom regions in

southern hemisphere (SH) like South America and Africa were not considered for the comparison due to very low representation of the CO_2 observation vector over these regions.

Station map for MLEF

year 2009

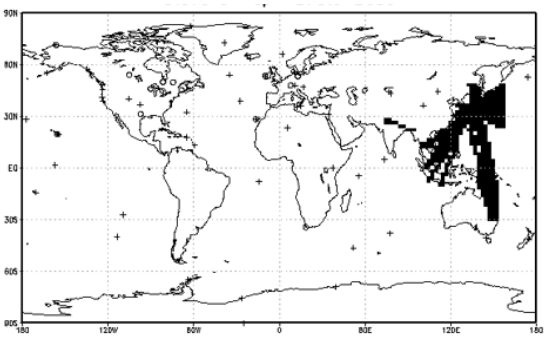

Open circles – continuous sites
Crosses – flask sampling sites
Dark squares – CONTRAIL tracks

year 2010

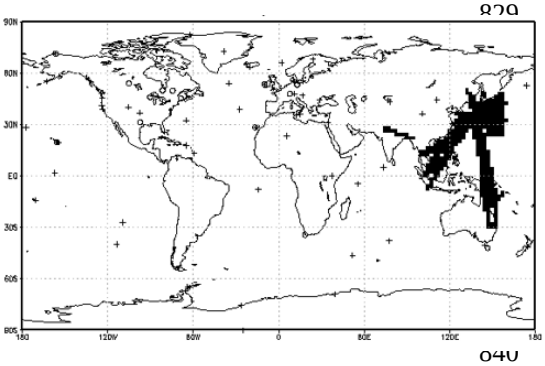

year 2011

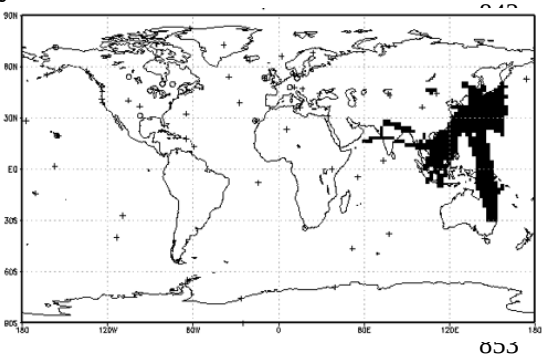

Station map for CT2017

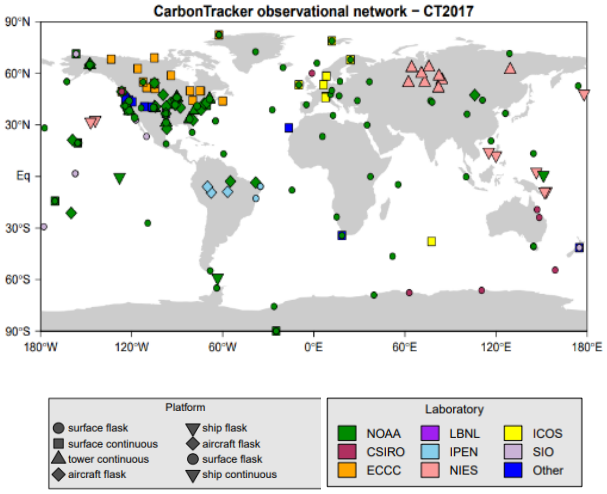

Figure 10. Stations map for MLEF (Left panel) and CT2017 (Right panel)

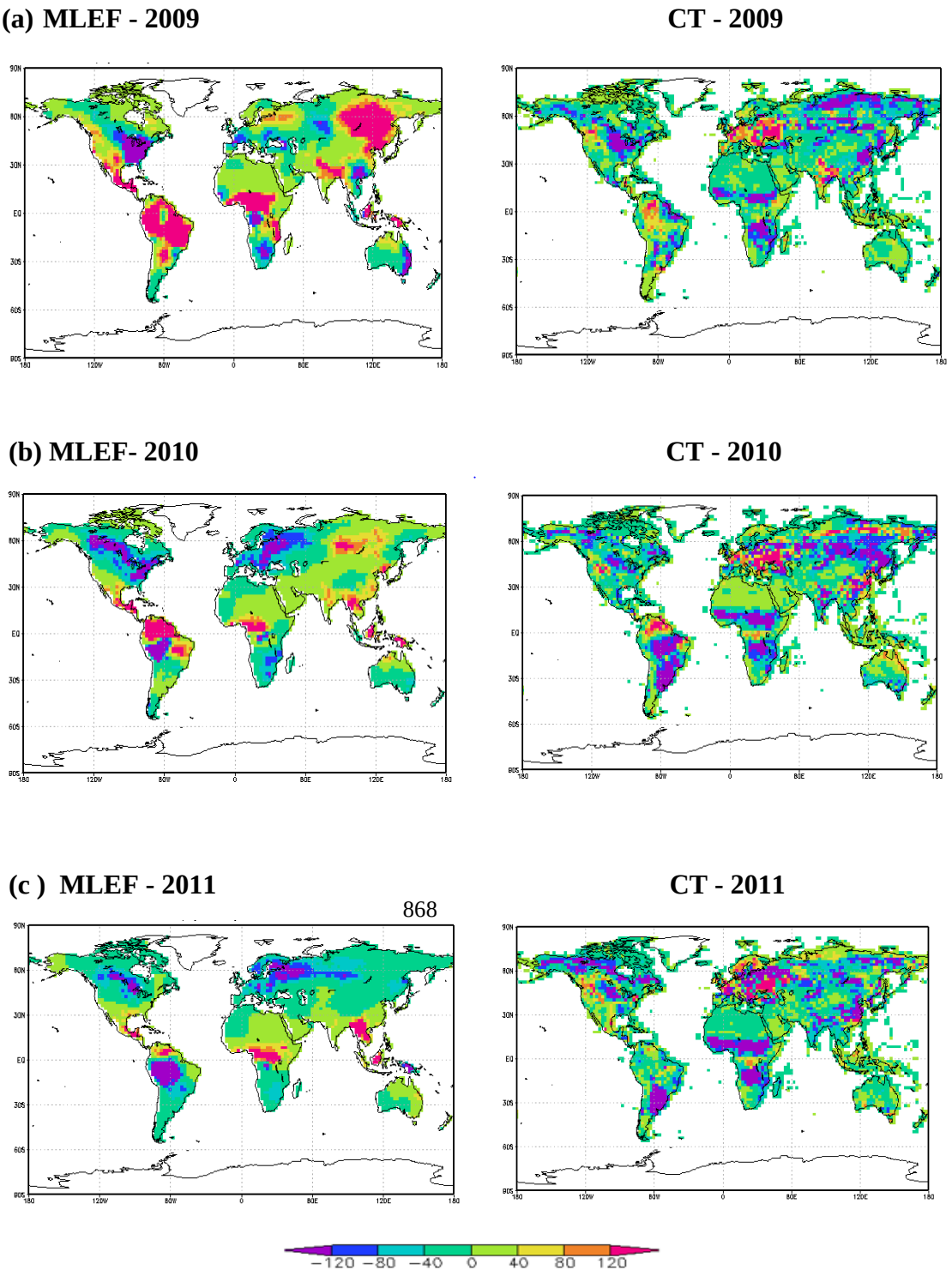

Figure 11. Recovered Mean Annual NEE by MLEF (Left panel) and CT (CT2017) (Right panel) for the year (a) 2009, (b) 2010 and (c) 2011 respectively. Units: gC m^{-2} yr^{-1}.

According to Figure 11, spatial patterns of the estimated terrestrial biosphere fluxes for the TransCom regions show quite different results. The CO_2 observation vector used for the two inversion methods are different. This may be the reason for different spatial patterns in some regions (Figure 11). Optimized biosphere fluxes form MLEF and CarbonTracker and the prior used are summarized in Table 4 and Figure 12.

Table 4. Optimized surface CO_2 fluxes and their one-sigma uncertainties ($PgCyr^{-1}$) for the selected TransCom regions from 2009 to 2011using MLEF and CT2017 method

Region	2009		2010		2011	
	MLEF	CT	MLEF	CT	MLEF	CT
Boreal N. America	-0.004 ± 0.16	-0.30 ± 0.76	-0.427 ± 0.26	-0.37 ± 0.9	-0.27 ± 0.11	-0.62 ± 0.87
Temperate N. America	-0.476 ± 0.23	-0.50 ± 0.53	-0.296 ± 0.27	-0.3 ± 0.36	-0.045 ± 0.073	-0.05 ± 0.4
Tropical Asia	0.148 ± 0.29	-0.07 ± 0.37	0.44 ± 0.24	-0.02 ± 0.36	0.609 ± 0.146	0.07 ± 0.29
Australia	-0.142 ± 0.18	-0.04 ± 0.3	-0.002 ± 0.097	-0.01 0± 0.41	0.033 ± 0.047	-0.04 ± 0.33
Eurasian Temperate	0.570 ± 0.38	-0.07 ± 0.37	0.227 ± 0.17	-0.62 ± 1.55	0.096 ± 0.10	-0.97 ± 1.67
Europe	-0.036 ± 0.33	0.37 ± 1.77	-0.662 ± 0.35	0.08 ± 2.12	-0.576 ± 0.194	-0.17 ± 1.89
Land Total	5.648	-3.33 ± 4.19	0.741	4.55±4.03	-1.169	-4.91±3.97
Ocean Total	-1.430	-3.13 ± 1.45	-1.448	-2.26±1.40	-1.511	-2.80±1.07

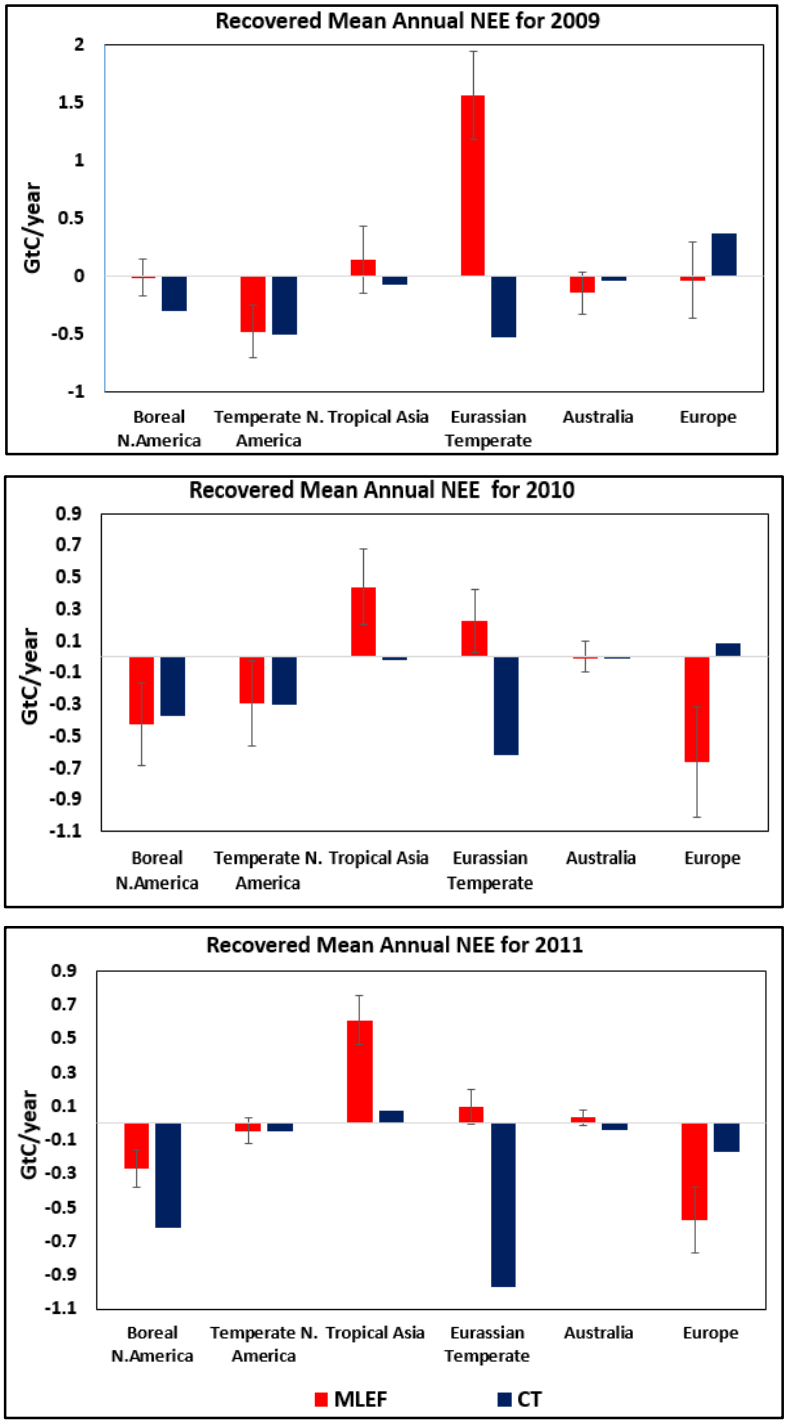

Figure 12. Mean annual NEE with 1-σ error bars aggregated to TransCom regions; Boreal North America, Temperate North America, Europe, Tropical Asia, Eurasian Temperate and Australia, estimated by MLEF and CarbonTracker (a) for 2009, (b) for 2010 and (c) for 2011. Units: GtC/year.

Spatial distribution of the mean annual CO_2 land fluxes derived from MLEF over North American region and several parts of the Asian region, like South Asia and Southeast Asia show good agreement with the CarbonTracker fluxes. South Asian region seems to be carbon

neutral for year 2011 and the observed carbon source pattern under CarbonTracker for year 2009 was also well captured by our model (Figure 11). Boreal North America and Temperate North America are highly rich in surface flask and continuous CO_2 measurement sites and those are carbon sinks with MLEF results, for the years from 2009-2011. This result shows good agreement with the CarbonTracker fluxes (Figure 11, 12). MLEF fluxes show that the Tropical Asia is a carbon source. But it is a weak sink for the years 2009 and 2010 and is a source for year 2011 under the CarbonTracker results. In our study, the selected CONTRAIL aircraft tracks mainly cover the regions of South Asia, Southeast Asia, East Asia and Australia (Figure 10). But, those regions are poorly represented in flask and continuous CO_2 measurement sites (see Figure 1). In CT2017, optimized fluxes for the above regions have the effect of densely available flask and continuous sampling sites than what we have used in MLEF method. This may be the reason for the difference between the optimized flux in Tropical Asia.

In Eurasian Temperate region, our optimized land fluxes for the period 2009-2011 (on average it is +0.53 $PgCyr^{-1}$) is different from CarbonTracker results (Figure 12) which shows it as a carbon sink. The reason for this difference may be the impact of the atmospheric CO_2 observation network we used. There are several flask and continuous observation sites covering the East Asia in CT2017 (Figure 10) than MLEF. In this study, Europe is a carbon sink for the years 2009-2011. According to CarbonTracker results it is a carbon source for the years 2009 and 2010 and a carbon sink for year 2011 (Figure 11). This difference may due to the effect of densely observed surface continuous CO_2 sites used in CT2017 rather than MLEF data assimilation (Figure 10).

MLEF solves for biases at the grid-scale and does not impose any prior spatial patterns into the fluxes (recall that the prior annual NEE in SiB is identically zero at every grid cell). Biomass emissions are not included in SiB priors. However, CarbonTracker solves for fluxes by prescribing spatial patterns according to eco-regions (Peters et al., 2005; 2007). The large basis regions used in CarbonTracker is beneficial in recovering fluxes over sparsely sampled regions; however, it restricts changes to the prescribed spatial flux patterns even in densely observed areas. However, the spatial distribution of the mean annual fluxes over North America, Australia and several regions in Asia derived from the MLEF and CarbonTracker show similar results when aggregated into large (TransCom) regions.

3.6 Comparison of optimized carbon fluxes with other studies

Comparison of the MLEF optimized CO_2 fluxes with other inverse modelling methods for the selected TransCom regions are summarized in Figure 13. MLEF results are mainly compared with the results of CT2017, Kim et al. (2017), Peylin et al. (2013) and Zhang et al. (2014) by considering the time period and the CO_2 observation network used for the optimization. Zhang et al. (2014) used CarbonTracker data assimilation method with surface and CONTRAIL measurements to obtain optimized fluxes for the years 2006-2010. Peylin et al. (2013) also used CarbonTracker method using flask and continuous CO_2 observations and obtained optimized carbon fluxes for TransCom regions for the years 2006-2010. The optimized fluxes by Peylin et al. (2013) were obtained from the online supplement (available online at http://www.biogeosciences.net/10/ 6699/2013/bg-10-6699-2013-supplement.pdf). Kim et al. (2017) also used CarbonTracker method to estimate carbon fluxes for the TransCom regions using Siberian observations during the years 2002-2009. In the next step, the spatial distribution of the optimized CO_2 fluxes in South Asian (which includes the countries Bangladesh, Bhutan, India, Nepal, Pakistan and Sri Lanka) region was compared with MLEF results considering

several studies in the literature (Patra et al., 2013, Jiang et al., 2014, and Thompson et al., 2016). Finally, the MLEF results obtained by assimilating surface and CONTRAIL CO_2 observations are compared with the results of inverse modelling studies which used surface and Greenhouse Gases Observing Satellite (GOSAT) total column CO_2 (XCO_2) observations for their flux inversion.

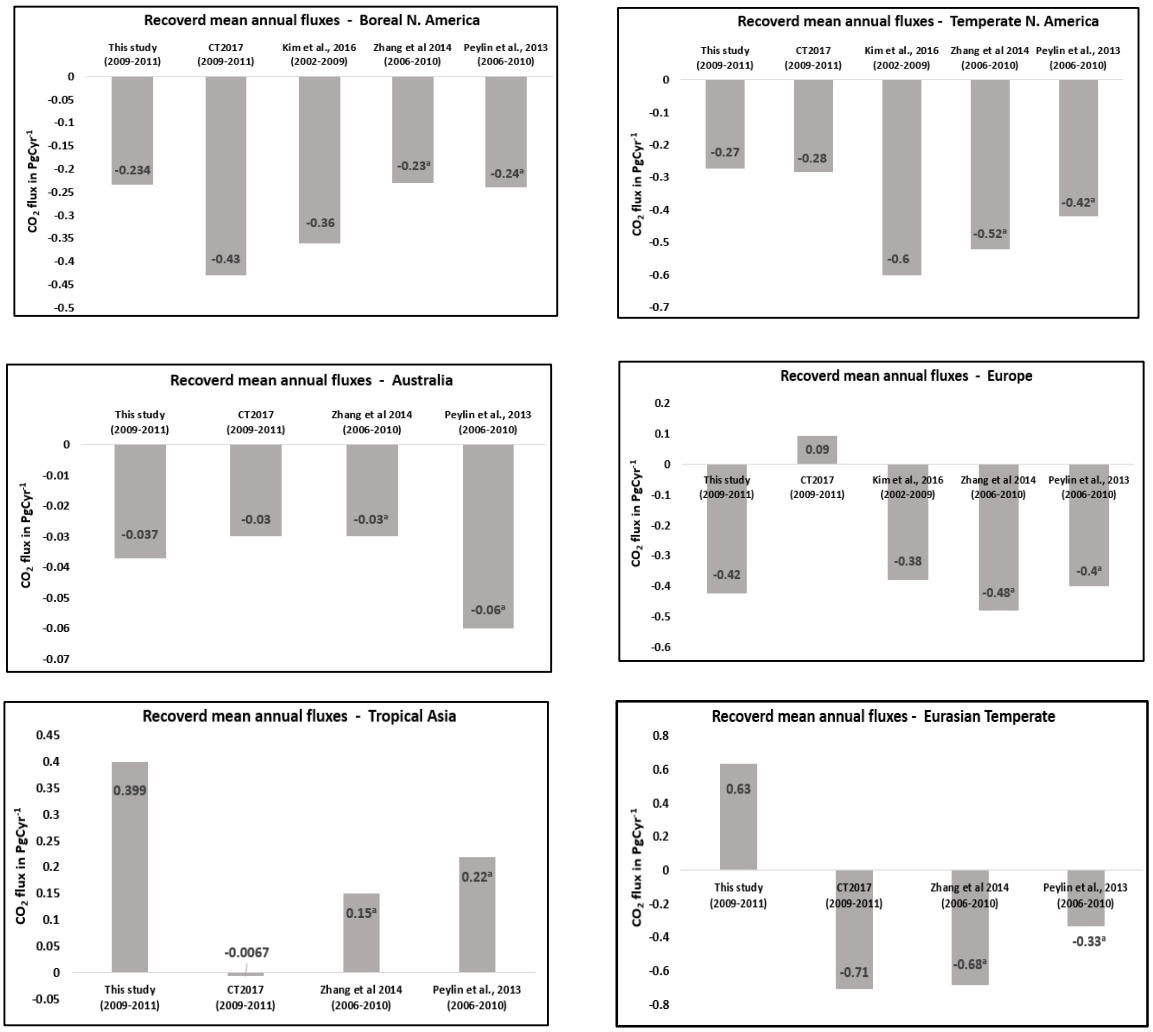

Figure 13. Comparison of optimized surface CO_2 fluxes (GtC yr^{-1}) from MLEF with other studies

[a]Biomass burning emissions are included into the land fluxes

Optimized carbon fluxes in other studies are summarized with MLEF optimized land fluxes and are given in Figure 13 (Note: In Zhang et al. (2014) and Peylin et al. (2013), the optimized fluxes include land and fire emissions). The average annual recovered fluxes from MLEF for Boreal North America (-0.234 $PgCyr^{-1}$), Temperate North America (-0.27 $PgCyr^{-1}$), Australia (-0.037 $PgCyr^{-1}$) and Europe (-0.42 $PgCyr^{-1}$) during the period from 2006-2010 (carbon sinks) are more comparable with the estimated fluxes in other selected studies.

1034 According to Zhang et al. (2014), mean terrestrial carbon uptake in Asia is -1.56 (= land fluxes
1035 + fire emissions) $PgCyr^{-1}$ which was further partitioned into -1.02 $PgCyr^{-1}$ carbon sink in Boreal
1036 Eurasia and -0.68 $PgCyr^{-1}$ carbon sink in Temperate Eurasia and a +0.15 $PgCyr^{-1}$ CO_2 source
1037 in Tropical Asia. Zhang et al. (2014) shows that posterior land flux for the Tropical Asia is -
1038 0.17 ± 0.28 $PgCyr^{-1}$ from 2006-2010. According to the MLEF results, Tropical Asia is a carbon
1039 source (+0.399 $PgCyr^{-1}$) from 2009-2011. Other than that, CT2017 also shows a weak sink (-
1040 0.0067 $PgCyr^{-1}$) for this region. The number of CONTRAIL-JAL aircraft tracks used in our
1041 study (from year 2009–2011) shows more coverage than the CONTRAIL used in Zhang et al.
1042 (2014) over Tropical Asian region (see Figure 10 and Figure1. (b) in Zhang et al., 2014). This
1043 may be the reason for this difference in Tropical Asian flux estimates. MLEF results show that
1044 the Eurasian Temperate is a carbon source (+0.63 $PgCyr^{-1}$) and this results is not compatible
1045 with other studies. The discrepancy between the results in Temperate Eurasia may be due to
1046 the CO_2 observation network used. Zhang et al. (2014), has more coverage of CONTRAIL
1047 observations over Boreal Eurasia to Europe (Figure1. (b) in Zhang et al., 2014) rather than the
1048 CONTRAIL CO_2 we used in our study. The CO_2 observation network used by Peylin et al.
1049 (2013) is the same as the CarbonTracker and it has more coverage of flask and continuous sites
1050 in Boreal and Temperate Eurasian regions. These observation networks reveal an insufficient
1051 observation coverage in this region and it may have an effect on the estimated land fluxes in
1052 Eurasian Temperate region. Finally, as an overall result, it can be said that the MLEF results
1053 with surface and CONTRAIL CO_2 observations show reasonable estimates for the selected
1054 TransCom regions when compared with the results of the studies discussed above.
1055
1056 Patra et al. (2013) has presented the net carbon budget for the South Asia for the period 1990-
1057 2009. Based on the atmospheric CO_2 inversions, it was found that net biospheric CO_2 flux in
1058 South Asia was a sink ($-104 \pm 150 TgC\ yr^{-1}$) during the period of 2007-2008. Jiang et al. (2014)
1059 estimated terrestrial CO_2 flux in China during 2002-2008 using an atmospheric inversion
1060 method with passenger aircraft-based CO_2 measurements over Eurasia. The results showed that
1061 with the addition of CONRATL CO_2 data, it increased the carbon sink in China from -
1062 0.16 ± 0.19 to -0.29 ± 0.18 $PgCyr^{-1}$ while decreasing the carbon sink in Southeast and South Asia
1063 by -0.68 ± 0.34 to -0.28 ± 0.32 and -0.35 ± 0.30 to -0.11 ± 0.30 $PgCyr^{-1}$, respectively. Thompson et
1064 al. (2016) assessed the carbon budget of Asia under seven atmospheric CO_2 inversions focusing
1065 East, South and Southeast Asian regions. According to the results from the inversion ensemble,
1066 Thompson et al. (2016) found that the land biosphere in South Asia was close to being carbon
1067 neutral with a flux of -0.05 (-0.18 to 0.03) PgC per year for the period 1996-2012. The surface
1068 carbon flux for South Asian region was not quantified in this study. But, the spatial distribution
1069 of the MLEF carbon flux in South Asian region shows more compatible results with the
1070 CT2017 results (Figure 11) and other selected studies.
1071
1072 Saeki et al. (2013) conducted an inverse modelling analysis to estimate the surface carbon flux
1073 using column-averaged dry air mole fractions of CO_2 observed by the GOSAT (which started
1074 to record observations from year 2009) and ground based data from June 2009 to October 2010.
1075 The results showed that the annual total sink for the South Asian region (June 2009-May 2010)
1076 was 0.23 $PgC\ yr^{-1}$ from NOAA data inversion, while NOAA plus GOSAT gave a stronger sink
1077 of 0.48 $PgC\ yr^{-1}$. GOSAT XCO_2 contains information about the free and upper troposphere like
1078 CONTRAIL CO_2 measurements (Basu et al., 2014). Basu et al. (2014), estimated CO_2 flux
1079 over Tropical Asia in 2009, 2010 and 2011 using RemoTec v2.11 retrievals of GOSAT XCO_2
1080 and surface measurements of CO_2, using four-dimensional variational (4DVAR) atmospheric
1081 inversion using the atmospheric tracer transport model TM5. According to the surface CO_2
1082 flux per 3 month time window obtained (Basu et al., 2014-Figure 2), Tropical Asia seems to
1083 be a source from GOSAT estimates. This results is more compatible with MLEF result for

Tropical Asia which is a carbon source (Figure 12). According to Basu et al. (2014), this increased source estimate is consistent with CONTRAIL measurements. Basu et al. (2013), optimized global source-sink estimates using surface and GOSAT CO_2 data from 1st September 2009 to 1st September 2010 and the results can be compared with MLEF results with surface and CONTRAIL observations. According to Basu et al. (2013), North American prior source (0.4 ± 0.5 PgC) converted to a posterior sink (0.4 ± 0.20 PgC) using surface data and this sink was strengthened by 1.0 ± 1.0 PgC using surface and GOSAT data. Prior source (0.3 ± 0.40 PgC) of the Europe, converted to a sink (0.3 ± 0.30 PgC) by surface data and with addition of GOSAT strengthened the sink by 1.3 ±0.20 PgC. Eurasian temperate region is a sink (0.1 ±0.20 PgC) with surface data and it was a source (0.3 ±0.20 PgC) with both measurements. Prior source (0.3 ±0.7 PgC) for the tropics is increased by surface data to 0.5 ±0.4 PgC and it was further increased to 2.1 ±0.20 PgC by adding GOSAT. Estimated posterior for North America, Europe and Eurasian Temperate with surface and GOSAT data in Basu et al. (2013) are comparable with the posterior fluxes estimated using surface and CONTRAIL data using MLEF (Figure 12).

4 Conclusions

This paper presents the first application of the MLEF method to assimilate existing flasks, continuous observations and CONTRAIL measurements. Previously, this assimilation system was tested with a pseudo-data experiment, which showed satisfactory results over the densely observed areas (Lokupitiya et al., 2008; Perera et al., 2017). In this study, flux estimation is done by separating NEE into GPP and respiration components and hence is potentially useful in identifying the driving forces of the carbon sinks. Currently, however, the daytime atmospheric CO_2 observations that we assimilate cannot be adequately separated into these two components. Nighttime CO_2 observations contain information about respiration, but the transport models poorly represent the nighttime values. In order to separate these components, additional constraints could be added to the model, such as carbonyl sulfide as a tracer of GPP (Lokupitiya et al., 2008).

In this paper, we have given flux estimates for densely observed North America, Europe and Asia, where we expect the observation network to provide additional constraints for years 2009-2011. A comparison of the results with another similar technique, CarbonTracker (CT2017), shows good agreement at large (TransCom) regional scale. However, spatial patterns are quite different, which seem to be dominated by the differences in prior assumptions, especially the hard constraint of ecosystem classification used to scale net fluxes in CarbonTracker. The grid scale inversion setup that we considered here can produce satisfactory annual mean flux estimates over the densely observed regions. However, the recovered fluxes at grid scale over sparsely sampled regions are not reliable. The method recovers fluxes in North America, Asia and Europe with less uncertainty. North America shows about 60-80% uncertainty reduction. Moderate results are obtained over the Asian and European region with about 50-60% uncertainty reduction. Most other land and oceanic regions show less than 30% uncertainty reduction. Recovery from the oceanic regions has high uncertainties because currently available atmospheric observations poorly constrain the weaker oceanic fluxes.

MLEF results with surface and CONTRAIL CO_2 observation network are more similar with other studies which used surface observations, surface plus CONTRAIL observations, surface plus Siberian observations and surface plus GOSAT observations in the CO_2 observation vector. Optimized fluxes in Temperate North America, Boreal North America, Australia, Europe and Tropical Asia are comparable with optimized fluxes with other studies. However,

we found several discrepancies in the spatial distribution of the optimized fluxes and estimated flux for some TransCom regions. In flux inversions, the optimized fluxes mainly depend on several factors such as prior guess, transport model used, CO_2 observation network, etc. These may be the main reasons for the above incompatibilities.

The main conclusion that can be drawn from this study is that grid scale inversions can produce satisfactory regional results when aggregated into larger regions, given the regions are densely observed in space and time. Fluxes in more sparsely observed regions in southern hemisphere like Africa and South America were poorly recovered from the MLEF method. The decomposition of net terrestrial fluxes into gross fluxes driven by well understood fast processes and the focus of statistical power from the observations on the poorly understood slow biogeochemistry allow the regional flux estimation from current networks without the need for hard constraints in the form of ecosystem maps or assumed covariance structures used in previous studies.

MLEF performs well with high dimensional observation vectors and does not require computationally intensive sequential assimilation schemes. Hence, it is more suitable for assimilation of satellite retrievals. As networks of continuous observing sites, aircraft sampling, and satellite observing systems will emerge in the coming years, this framework can be easily extensible to those much larger data vectors. In a future paper, this assimilation system will be used to assimilate satellite observations from GOSAT and/or OCO2 projects.

Acknowledgments

This research is supported by the grants from NRC-Sri Lanka (National Research Council, Sri Lanka) (NRC-036) and APN (Asia-Pacific Network for Global Change Research; grant#ARCP2011-11NMY-Patra/Canadell). We gratefully acknowledge the computer support provided by Matt Bishop, Department of Atmospheric Science, Colorado State University, Fort Collins, Colorado, USA, Harsha Munasingha and Suresh Nanayakkara, Centre for IT Services, University of Sri Jayewardenepura, Sri Lanaka and Nuwan De Silva, Softlogic IT, Sri Lanka. CO_2 measurements used in this study are available from World Data Center for Greenhouse Gases (http://gaw.kishou.go.jp/) and the ObsPack data product (https://www.esrl.noaa.gov/gmd/ccgg/obspack/). We kindly acknowledge all atmospheric data providers to the GMD (Global Monitoring Division) data archive, NOAA/ESRL and those that contribute their data to WDCGG site and the CONTRAIL PIs Toshinobu Machida, Hidekazu Matsueda, Yousuke Sawa and Yosuke Niwa. We appreciate the CarbonTracker 2017 results obtained by NOAA ESRL, Boulder, Colorado, USA from the website (http://carbontracker.noaa.gov/) and MERRA-2 weather data downloaded from https://disc.gsfc.nasa.gov/, managed by the NASA Goddard Earth Sciences (GES) Data and Information Services Center (DISC) for our study.

References

Al-Ghussain, L. (2018). Global Warming: Review on Driving Forces and Mitigation. *Environmental Progress & Sustainable Energy*, 38(1), 13-21. https://doi.org/10.1002/ep

Baker, I., Denning, A. S., Hanan, N., Prihodko, L., Uliasz, M., Vidale, P. L., Daviss, K., & Bakwin, P. (2003). Simulated and observed fluxes of sensible and latent heat and CO_2 at the WLEF-TV Tower using SiB2.5. *Global Change Biology*, 9, 1262-1277. https://doi.org/10.1046/j.1365-2486.2003.00671.x

Baker, D. F., Doney, S. C., & Schimel, D. S. (2006). Variational data assimilation for atmospheric CO_2. *Tellus (2006)*, 58B, 359-365. https://doi: 10.1111/j.1600-0889.2006.00218.x

Basu, S., Guerlet, S., Butz, A., Houweling, S., Hasekamp, O., Aben, I., Krummel, P., Steele, P., Langenfelds, R., Torn, M., Biraud, S., Stephens, B., Andrews, A., & Worthy, D. (2013). Global CO_2 fluxes estimated from GOSAT retrievals of total columnCO_2. *Atmos. Chem. Phy*s., 13, 8695–8717. https://doi:10.5194/acp-13-8695-2013.

Basu, S., Krol, M., Butz, A., Clerbaux, C., Sawa, Y., Machida, T., Matsueda, H., Frankenberg, C., Hasekamp, O. P., & Aben, I. (2014). The seasonal variation of the CO2 flux over Tropical Asia estimated from GOSAT, CONTRAIL, and IASI. *Geophys. Res. Lett*., 41, 1809–1815, doi:10.1002/2013GL059105

Brenkert, A. (1998). Carbon dioxide emission estimates from fossil-fuel burning, hydraulic cement production, and gas flaring for 1995 on a one-degree grid cell basis. *Tech Rep NDP-058A*, Carbon Dioxide Information Analysis Center, Oak Ridge Natl. Lab., Oak Ridge, Tenn. (Available at http://cdiac.ess-dive.lbl.gov/newsletr/fall98/ccf98.pdf).

Bruhwiler, L. M. P., Michalak, A. M., Peters, W., Baker, D. F., & Tans, P. (2005). An improved Kalman Smoother for atmospheric inversions. *Atmospheric Chemistry and Physics*, 5, 2691-2702. https://doi.org/10.5194/acp-5-2691-2005

Bosilovich, M. G., Lucchesi, R., & Suarez, M. (2016). *MERRA-2: File Specification*. GMAO Office Note No. 9 (Version 1.1), 73 pp, available from http://gmao.gsfc.nasa.gov/pubs/office_notes.

CarbonTracker CT2017. Retrieved from https://www.esrl.noaa.gov/gmd/ccgg/carbontracker/CT2017/.

Chatterjee, A. (2012). *Data Assimilation for Atmospheric CO2: Towards Improved Estimates of CO2 Concentrations and Fluxes*, (Doctoral Dissertation, University of Michigan). Retrieved from Deep Blue. (https://deepblue.lib.umich.edu/handle/2027.42/96172).

Chatterjee, A., Michalak, A. M., Anderson, J. L., Mueller, K. L., & Yadav, V. (2012). Toward reliable ensemble Kalman filter estimates of CO_2 fluxes. *Journal of Geophysical Research*, 117, D22306. htpps://doi:10.1029/2012JD018176

Chevallier F., Fisher M., Peylin P., Serrar S., Bousquet P., Bre´on, F.-M., Che´din A., & Ciais P. (2005). Inferring CO_2 sources and sinks from satellite observations: Method and application to TOVS data. *Journal of Geophysical Research*, 110, D24309. https:/doi:10.1029/2005JD006390.

GLOBALVIEW-CO2. Retrieved from https://www.esrl.noaa.gov/gmd/ccgg/obspack/.

Gurney, K. R., Law, R. M., Denning, A. S., Rayner, P. J., Baker, D., Bousquet, P., Bruhwiler, L., Chen, Ciais, Y. H., P., Fan, S., Fung, I. Y., Gloor, M., Heimann, M., Higuchi, K., John, J., Maki, T., Maksyutov, S., Masarie, K., Peylin, P., Prather, M., Pak, B. C., Randerson, J., Sarmiento, J., Taguchi, S., Takahashi, T., & Yuen, C. W. (2002). Towards robust regional estimates of CO_2 sources and sinks using atmospheric transport models. *Nature*, 415, 626-630.

Feng, L., Palmer, P. I., B osch H., & Dance, S. (2009). Estimating surface CO_2 fluxes from space-borne CO_2 dry air mole fraction observations using an ensemble Kalman Filter. *Atmos. Chem. Phys*., 9, 2619–2633. https://doi.org/10.5194/acp-9-2619-2009

Jiang F., Wang, H. W., Chen, J. M., Zhou, L. X., Ju. W. M., Ding, A. J., Liu, L. X., & Peters, W. (2013). Nested atmospheric inversion for the terrestrial carbon sources and sinks in China. *Biogeosciences*, 10, 5311–5324. https://doi:10.5194/bg-10-5311-2013

Jiang, F., Wang, H. M., Chen, J. M., Machida, T., Zhou, L. X., Ju, W. M., Matsueda, H., & Sawa, Y. (2014). Carbon balance of China constrained by CONTRAIL aircraft CO_2 measurements. *Atoms. Chem. Phys*., 14, 10133-10144. https:// doi:10.5194/acp-14-10133-2014

Kaminski, T., Rayner, P. J., Heimann, M., & Entin, I. G. (2001). On aggregation errors in atmospheric transport inversions. *Journal of Geophysical Research*, 106, 4703-4715. https://doi.org/10.1029/2000JD900581

Kang, J. S., Kalnay, E., Liu, J., Fung, I., Miyoshi, T., & Ide, K. (2011). "Variable localization" in an ensemble Kalman filter: Application to the carbon cycle data assimilation. *Journal of Geophysical Research*, 116, D09110. https://doi:10.1029/2010JD014673

Kawa, S. R., Erickson III, D. J., Pawson, S., & Zhu, Z. (2004). Global CO_2 transport simulations using meteorological data from the NASA data assimilation system. Journal of Geophysical Research, 109, D18312, https://doi: 10.1029/2004JD004554.

Kim, J., Kim, H. M., & Cho, C., (2014). Influence of CO_2 observations on the optimized CO_2 flux in an ensemble Kalman filter. *Atmos. Chem. Phys*., 14, 13515–13530. https://doi.org/10.5194/acp-14-13515-2014

Kim, J., Kim, H. M., Cho, C., Boo, K., Jacobson, A. R., Sasakawa, M., Machida, T., Arshinov, M., & Fedoseev, N., (2017). Impact of Siberian observations on the optimization of surface CO_2 flux. *Atmos. Chem. Phys*., 17, 2881–2899. http:// doi:10.5194/acp-17-2881-2017

Kondo, M., Patra, P.K., Sitch, S., Friedlingstein, P., Poulter, B., Chevallier, F., Ciais, P., Canadell., J. G., Bastos, A., Lauerwald, R., Calle, L., Ichii, K., Anthoni, P., Arneth, A., Haverd, V., Jain, A. K., Kato, E., Kautz, M., Law, R.M., Lienert, S., Lombardozzi, D., Maki, T., Nakamura, T., Peylin, P., Rödenbeck, C., Zhuravlev, R., Saeki, T., Tian, H., Zhu, D., & Ziehn, T. (2019). State of the science in reconciling top-down and bottom-up approaches for terrestrial CO2 budget, *Glob Change Biology*, 1-17. https://doi: 10.1111/gcb.14917

Le Quéré, C., Andrew, R. M., Friedlingstein, P., Sitch, S., Hauck, J., Pongratz, J., Pickers, P. A., Korsbakken, J. I., Peters, G. P., Canadell, J. G., Arneth, A., Arora, V. K., Barbero, L., Bastos, A., Bopp, L., Chevallier, F., Chini, L. P., Ciais, P.,. Doney, S. C., Gkritzalis, T., Goll, D. S., Harris, I., Haverd, V., Hoffman, F. M., Hoppema, M., Houghton, R. A., Hurtt, G., Ilyina, T., Jain, A. K., Johannessen, T., Jones, C. D., Kato, E., Keeling, R. F., Goldewijk, K. K., Landschützer, P., Lefèvre, N., Lienert, S., Liu, Z., Lombardozzi, D., Metzl, N., Munro, D. R., Nabel, J. E. M. S., Nakaoka, Shin-ichiro., Neill, C., Olsen, A., Ono, T., Patra, P., Peregon, A., Peters, W., Peylin, P., Pfeil, B., Pierrot, D., Poulter, B., Rehder, G., Resplandy, L., Robertson, E., Rocher, M., Rödenbeck, C., Schuster, U., Schwinger, J., Séférian, R., Skjelvan, I.,

Steinhoff, T., Sutton, A., Tans, P. P., Tian, H., Tilbrook, B., Tubiello, F. N., Laan-Luijkx, Ingrid T. van der., Werf, Guido R. van der., Viovy, N., Walker, A. P., Wiltshire, A. J., Wright, R., Zaehle, S., & Zheng, B. (2018). Global Carbon Budget 2018. *Earth Syst. Sci. Data*, 10, 2141–2194. https://doi.org/10.5194/essd-10-2141-2018

Lokupitiya, R. S., Zupanski, D., Denning, A. S. Kawa, S. R., Gurney, K. R., & Zupanski, M. (2008). Estimation of global CO_2 fluxes at regional scale using the maximum likelihood ensemble filter. *Journal of Geophysical Research*. 113, D20110. http://doi:10.1029/2007JD009679.

Michalak, A. M., Bruhwiler, L., & Tans, P. P. (2004). A geostatistical approach to surface flux estimation of atmospheric trace gases. *Journal of Geophysical Research*. 109, D14109. https://doi:10.1029/2003JD004422.

Miyazaki, K., Maki, T., Prabir, P., & Nakazawa, T. (2011), Assessing the impact of satellite, aircraft, and surface observations on CO_2 flux estimation using an ensemble-based 4-D data assimilation system. *Journal of Geophysical Rerearch*, 116. D16306. https://doi:10.1029/2010JD015366

Machida, T., Matuseda, H., Sawa, Y., Nakagawa, Y., Hirotani, K., Kondo, N., Goto, K., Nakazawa, T., Ishikawa, K., Ogawa, T. (2008). Worldwide Measurements of Atmospheric CO_2 and Other Trace Gas Species Using Commercial Airlines. *Journal of Atmospheric and Oceanic Technology.*, 25, 1744–1754, htttps://doi: http://dx.doi.org/10.1175/2008JTECHA1082.1.

Matsueda, H., Machida, T., Sawa, Y., Nakagawa, Y., Hirotani, K., Ikeda, H., Kondo, N., & Goto, K.. (2008). Evaluation of atmospheric CO2 measurements from new flask air sampling of JAL airliner observations. *Meteorology and Geophysics*, 59, 1-17. https:// doi:10.2467/mripapers.59.1

Niwa, Y., Patra, P. K., Sawa, Y., Machida, T., Matsueda, H., Belikov, D., Maki, T., Ikegami, M., Imasu, R., Maksyutov, S., Oda, T., Satoh, M., & Takigawa, M. (2011). Three-dimensional variations of atmospheric CO_2: aircraft measurements and multi-transport model simulations. *Atmos. Chem. Phys*., 11, 13359–13375. https://doi:10.5194/acp-11-13359-2011.

Niwa, Y., Machida, T., Sawa, Y., Matsueda, H., Schuck, T. J., Brenninkmeijer, C. A. M., Imasu, R., & Satoh, M. (2012). Imposing strong constraints on tropical terrestrial CO_2 fluxes using passenger aircraft based measurements. *Journal of Geophysical. Research*, 117, D11303. https://doi:10.1029/2012JD017474.

Patra, P. K., Law R. M., Peters W., Ro¨denbeck C., Takigawa M., Aulagnier C., Baker I., Bergmann, D. J., Bousquet, P., Brandt, J., Bruhwiler, L., Smith, P. J. C., Christensen, J. H., Delage, F., Denning, A. S., Fan, S., Geels, C., Houweling, S., Imasu, R., Karstens, U., Kawa, S. R., Kleist, J., Krol, M. C., Lin, S.-J., Lokupitiya, R., Maki, T., Maksyutov, S., Niwa, Y., Onishi, R., Parazoo, N., Pieterse, G., Rivier, L., Satoh, M., Serrar, S., Taguchi, S., Vautard, R., Vermeulen, A. T., & Zhu Z. (2008). TransCom model simulations of hourly atmospheric CO_2: Analysis of synoptic-scale variations for the period 2002-2003. *Global Biogeochemical Cycles*, 22, GB4013. https:/doi:10.1029/2007GB003081

Patra, P. K., Niwa, Y., Schuck, T. J., Brenninkmeijer, C. A. M., Machida, T., Matsueda, H., & Sawa, Y. (2011). Carbon balance of South Asia constrained by passenger aircraft CO_2 measurements. *Atmos. Chem. Phys.*, 11, 4163-4175. https:// doi:10.5194/acp-11-4163-2011

Patra, P. K., Canadell, J. G., Houghton, R. A., Piao, S. L., Oh, N.-H., Ciais, P., Manjunath, K. R., Chhabra, A., Wang, T., Bhattacharya, T., Bousquet, P., Hartman, J., Ito, A., Mayorga, E., Niwa, Y., Raymond, P., Sarma, V. V. S. S., & Lasco, R. (2012), The carbon budget of South Asia. *Biogeosciences Discuss*., 9, 13537–13580. http://doi:10.5194/bgd-9-13537-2012

Patra, P. K., Canadell, J. G., Houghton, R. A., Piao, S. L., Oh, N. –H., Ciais, P., Manjunath, K. R., Chhabra, A., Wang, T., Bhattacharya, T., Bousquet, P., Hartman, J., Ito, A., Mayorga, E., Niwa, Y., Raymond, P. A., Sarma, V. V. S. S., & Lasco, R. (2013). The carbon budget of South Asia. *Biogeosciences*, 10, 513-527. https:// doi:10.5194/bg-10-513-2013

Perera, K.M.P., Lokupitiya, R.S., Zupanski, D., Denning, A.S., Meegama, R.G.N., Lokupitiya, E.Y.K., & Patra, P.K. (2017). *Estimation of Asian and Global Carbon Fluxes Using Maximum Likelihood Ensemble Filter (MLEF),* Paper presented at International Conference on Climate Change - 2017, Colombo, Sri Lanka.

Peters, W., Miller, J. B., Whitaker, J., Denning, A. S., Hirsch, A., Krol, M. C., Zupanski, D., Bruhwiler, L., & Tans, P. P. (2005). An ensemble data assimilation system to estimate CO_2 surface fluxes from atmospheric trace gas observations. *Journal of Geophysical Research*, 110, D24304. https://doi:10.1029/2005JD006157.

Peters, W., Jacobson, A. R., Sweeney, C., Andrews, A. E., Conway, T. J., Masarie, K., Miller, J. B., Bruhwiler, L. M. P., Pétron, G., Hirsch, A. I., Worthy, D. E. J., Werf, G. R. van der, Randerson, J. T., Wennberg, P. O., Krol, M. C., & Tans, P. P. (2007). An atmospheric perspective on North American carbon dioxide exchange: CarbonTracker. *PNAS*, 104, 18925-18930. https://www.pnas.org/content/pnas/104/48/18925.full.pdf

Peylin, P., Law, R. M., Gurney, K. R., Chevallier, F., Jacobson, A. R., Maki, T., Niwa, Y., Patra P. K., Peters, W., Rayner, P. J., Rödenbeck, C., van der Laan-Luijkx, I. T., & Zhang, X. (2013). Global atmospheric carbon budget: results from an ensemble ofatmospheric CO_2 inversions. *Biogeosciences*, 10, 6699–6720. https://doi:10.5194/bg-10-6699-2013

Piao, S., Fang, J., Ciais, P., Peylin, P., Huang, Y., Sitch, S., & Wang, T. (2009). The carbon balance of terrestrial ecosystems in China. *Nature*, 458, 1009-1013. https://doi: 10.1038/nature07944

Piao, S. L., Ito, A., Huang, S. G. Li, Y., Ciais, P., Wang, X. H., Peng, S. S., Nan, H. J., Zhao, C., Ahlstr¨om, A., Andres, R. J., Chevallier, F., Fang, J. Y., Hartmann, J., Huntingford, C., Jeong, S., Levis, S., Levy, P. E., Li, J. S., Lomas, M. R., Mao, J. F., Mayorga, E., Mohammat, A., Muraoka, H., Peng, C. H., Peylin, P., Poulter, B., Shen, Z. H., Shi, X., Sitch, S., Tao, S., Tian, H. Q., Wu, X. P., Xu, M., Yu, G. R., Viovy, N., Zaehle, S., Zeng, N., & Zhu, B. (2012).The carbon budget of terrestrial ecosystems in East Asia over the last two decades. *Biogeosciences*, 9, 3571–3586. https:// doi:10.5194/bg-9-3571-2012

Ro¨denbeck, C., Houweling, S., Gloor, M., & Heimann, M. (2003). CO_2 flux history 1982–2001 inferred from atmospheric data using a global inversionof atmospheric transport. *Atmos. Chem. Phys*., 3, 1919–1964. https://doi.org/10.5194/acp-3-1919-2003

Saeki, T., Maksyutov, S., Saito, M., Valsala, V., Oda, T., Andres, R. J., Belikov, D., Tans, P., Dlugokencky, E., Yoshida, Y., Morino, I., Uchino, O., & Yokota, T. (2013). Inverse Modeling of CO2 Fluxes Using GOSAT Data and Multi-Year Ground-Based Observations. *SOLA*, 9, 45−50. https://doi:10.2151/sola.2013-011

Sajeev, P., Johnson, M. S., Potter, C., Genovesse, V., Baker, D. F., Haynes, K. D., Henze, D. K., Liu J., & Poulter, B. (2019). Prior biosphere modelimpacton global terrestrial CO2 fluxes estimated from OCO-2 retrievals. *Atmos. Chem. Phys*, 19, 13267–13287. https://doi.org/10.5194/acp-19-13267-2019

Sawa, Y., Machida, T., & Matsueda, H. (2012). Aircraft observation of the seasonal variation in the transport of CO_2 in the upper atmosphere. Journal of Geophysical Research, 117, D05305. https://doi:10.1029/2011JD016933.

Schuh, A. E., Denning, A. S., Corbin, K. D., Baker, I. T., Uliasz, M., Parazoo, N., Andrews, A. E., & Worthy, D. E. J. (2010). A regional high-resolution carbon flux inversion of North America for 2004. *Biogeosciences*, 7, 1625–1644, https://doi:10.5194/bg-7-1625-2010

Tans, P. P., Fung, I. Y., & Takahashi, T. (1990). Observational constraints on the global atmospheric CO_2 budget . *Science*, 247, 1431-1438. http://links.jstor.org/sici?sici=0036-8075%2819900323%293%3A247%3A4949%3C1431%3AOCOTGA%3E2.0.CO%3B2-N

Thompson, R.L., Patra, P.K., Chevallier, F., Maksyutov, S., Law, R.M., Ziehn, T., Luijkx, I.T. van der Laan, Peters, W., Ganshin, A., Zhuravlev, R., Maki, T., Nakamura, T., Shirai, T., Ishizawa, M., Saeki, T., Machida, T., Poulter, B., Canadell, J. G. & Ciais, P. (2016). Top–down assessment of the Asian carbon budget since the mid 1990s. *Nature Communications*, 7:10724. https://doi: 10.1038/ncomms10724

Takahashi, T., Sutherland, S. C., Sweeney, C., Poisson, A., Metzl, N., Tilbrook, B., Bates, N., Wanninkhof, R., Feely, R. A., Sabine, C., Olafsson, J., & Nojiri, Y. (2002). Global sea-air CO_2 flux based on climatological surface ocean pCO_2, and seasonal biological and temperature effects. *Deep-Sea Res. Part II*, 49, 1601-1622. https://doi:10.1016/S0967-0645(02)00003-6

Whitaker, J. S., & Hamill, T. M., (2002). Ensemble Data Assimilation without Perturbed Observations. *Monthly Weather Review*, 130 (7), 1913–1924. https://doi.org/10.1175/1520-0493(2002)130<1913:EDAWPO>2.0.CO;2

Zhang, H. F., Chen, B. Z., Luijkx, I. T. van der L., Machida, T., Matsueda, H., Sawa, Y., Fukuyama, Y., Langenfelds, R., Schoot M. van der, Xu, G., Yan, J. W., Cheng, M. L., Zhou, L. X., Tans, P. P., & Peters W. (2014). Estimating Asian terrestrialcarbon fluxes from CONTRAIL aircraft and surface CO_2 observations for the period 2006–2010. *Atoms. Chem. Phys*., 14, 5807-5824. https:// doi:10.5194/acp-14-5807-2014

Zupanski, M. (2005). Maximum likelihood ensemble filter: Theoretical aspects. *Monthly Weather Review*, 133(6), 1710-1726. https://doi.org/10.1175/MWR2946.1

Zupanski, D., Denning, A. S., Uliasz, M., Zupanski, M., Schuh, A. E., Rayner, P. J., & Peters, W. (2007). Carbon flux bias estimation employing Maximum Likelihood Ensemble Filter (MLEF). *Journal of Geophysical Research*, 112, D17107. https:// doi:10.1029/2006JD008371.

Figure 1. A map of the continuous and flask stations used in this study except CONTRAIL. Open circles depict continuous measurement sites (see Table 1). Crosses identify flask-sampling locations that are part of the NOAA-ESRL network (GLOBALVIEW-CO2).

Figure 2. Variation of the observation errors for Continuous stations for the years 2009-2011.

Figure 3. Variation of the observation errors for Flask stations for the years 2009-2011.

Figure 4. Variation of the observation errors for CONTRAIL locations for the years 2009-2011.

Figure 5. Observed hourly CO_2 concentrations (in blue) and simulated CO_2 (in red) from PCTM for years from 2009 – 2011 at stations FSD (Fraserdale, Canada), AMT (Argyle, Maine, United States) and BRW (Barrow Atmospheric Baseline Observatory, United States).

Figure 6. Daily time series plots of CO_2 concentrations from posterior fluxes (in red) and prior fluxes (in black) compared to observations (in blue) for years 2009 – 2011 at Yonagunijima, Japan (YON), Ryori, Japan (RYO), Anmyeon-do, Republic of Korea (AMY), Argyle, Maine, United States (AMT), Chibougamau, Canada (CHM) and Anmyeon-do, Republic of Korea (AMY)

Figure 7. Variation of CONTAIL CO_2 observations with relevant altitude (m).

Figure 8. Distribution of the difference between observed CO_2 and recovered CO_2 under four vertical bins for years 2009 to 2011.

Figure 9. Stations map with CONTRAIL locations and mean annual percentage uncertainty reduction for the years (a) 2009, (b) 2010 and (c) 2011.

Figure 10. Stations map for MLEF (Left panel) and CT2017 (Right panel)

Figure 11. Recovered Mean Annual NEE by MLEF (Left panel) and CT (CT2017) (Right panel) for the year (a) 2009, (b) 2010 and (c) 2011 respectively. Units: gC m^{-2} yr^{-1}.

Figure 12. Mean annual NEE with 1-σ error bars aggregated to TransCom regions; Boreal North America, Temperate North America, Europe, Tropical Asia, Eurasian Temperate and Australia, estimated by MLEF and CarbonTracker (a) for 2009, (b) for 2010 and (c) for 2011. Units: GtC/year.

Figure 13. Comparison of optimized surface CO_2 fluxes (GtC yr^{-1}) from MLEF with other studies

[a]Biomass burning emissions are included into the land fluxes

1478 **Table 1.** Continuous and Flask CO_2 measurement sites used in this study

1479 **Table 2.** Root Mean Square Error (RMSE) with respect to the prior and the posterior at
1480 continuous sites for 2009 to 2011 Units: parts per million by volume (ppmv)

1481 **Table 3.** Root Mean Square Error (RMSE) with respect to the posterior CONTRAIL CO_2
1482 measurements for 2009 to 2011 Units: parts per million by volume (ppmv)

1483 **Table 4.** Optimized surface CO_2 fluxes and their one-sigma uncertainties ($PgCyr^{-1}$) for the
1484 selected TransCom regions from 2009 to 2011using MLEF and CT2017 method